THESIS

QUANTIFICATION OF FLUORESCENCE SIGNALS FROM 800CW-LABELLED TUMOUR TISSUE

Iris Schmidt
Technical Medicine - Medical Imaging and Intervention

Exam committee
Chair: Prof.Dr.Ir. C.H. Slump
Medical supervisor: Dr. W.B. Nagengast
Technical supervisor: Dr.Ir. H.L. Offerhaus
Process supervisor: R.J. Haarman, MSc
External supervisor: Dr. C. Blum

umcg

UNIVERSITY OF TWENTE.

Abstract

The aim of this study is to improve quantification of the measured fluorescence signal in surgical specimen to acquire a more objective observation of the fluorescence intensity and ultimately, make a clear distinction between tumorous and non-tumorous tissue. The primary objective of this study is to determine the feasibility of two quantification methods to make a clearer distinction between tumorous and non-tumorous tissue, by correcting the fluorescence signal for influences of illumination differences and tissue optical properties. Two correction methods are applied: a ratiometric correction method and space-variant deconvolution. For the ratiometric correction, a phantom is used for the validation for the correction for both the black box and intraoperative camera. Next, the correction method is applied to tissue images made with the black box. The space-variant deconvolution method is applied to both a mathematical phantom and black box images of tissue. Both methods show an improvement of the fluorescence detection. For the ratiometric correction, an improvement was visible for the phantom and the two tissue types, although the extent of the improvement differed between the three, due to image acquisition. This method could be applied clinically and improve clinical decision making based on fluorescent images. The results for the spatially-variant deconvolution showed that the method could improve fluorescence imaging, but involves multiple assumptions which could introduce inaccuracies in the resulting images. Therefore, the ratiometric correction proved to be a more solid correction method with short acquisition time compared to the spatially-variant deconvolution method. Additionally, the ratiometric correction would be easier to apply in a clinical, real time setting. For clinical incorporation, simultaneously acquired fluorescence and excitation images with automatic or predefined settings for polarization are crucial.

Acronyms

CNR contrast-to-noise ratio

MTF modulation transfer function

NIR near-infrared

NIR-MFGS Near-infrared molecular fluorescence guided surgery

OTF optical transfer function

PSF point spread function

ROI region-of-interest

SFDI spatial frequency domain imaging

SNR signal-to-noise ratio

TBR tumour-to-background ratio

UMCG University Medical Centre Groningen

Contents

1 | Introduction

1.1 Clinical background

1.1.1 Resection margins

Differentiation between tumorous and non-tumorous tissue is a crucial factor in oncology for diagnosis of (pre)malignant lesions, identification of treatment response to chemoradiotherapy and radical surgical resection. Currently, the golden standard for differentiation between tumorous and non-tumorous tissue is pathological examination of surgical specimen or biopsies, which, can only be performed after a procedure.

The main goal of surgery is complete resection of the tumour with clean surgical resection margins: no tumour cells present in the area surrounding the resection (figure 1.1). Clean resection margins are an important prognostic factor of local recurrence, distant metastases and overall survival in cancer [1,2]. To achieve complete removal of the tumour, surgeons resect surrounding tissues and structures to ensure tumour free resection margins. For circumferential resection, a margin of >1mm is defined and for other resections a margin of >2mm [3]. Although complete removal of the tumour is the primary goal, preservation of surrounding structures such as nerves and blood vessels are crucial as well. Therefore, tissue resection is sometimes limited to avoid significant damage to adjacent tissue. Preoperatively, a surgeon can rely on information from preoperative imaging modalities for differentiation between tumour and normal tissue. Intraoperatively, the surgeon can only rely on visual and tactile information and his/her experience. Unclear boundaries and microscopic, residual tumour spots complicate the differentiation between tumour and non-tumorous tissue and can lead to incomplete resections and thus positive resection margins or unnecessary removal of healthy tissue [4].

Multiple imaging modalities like (PET-)CT and MRI are well established techniques for the diagnosis and staging of cancer. However, their resolution is limited which hinders accurate detection of small tumour spots and deployment of these systems intraoperatively is difficult. The only option a surgeon has intraoperatively to verify clean resection margins is pathological examination of frozen tissue sections. However, examination of these frozen sections causes delay during surgery, they are expensive and can only be applied on a small fraction of the tissue [5]. If the surgeon is still unsure if clean resection margins are achieved, postoperative radiation therapy is possible to prevent recurrence of the tumour. However, radiation has significant side effects and increased morbidity. Ultimately, the verdict on positive surgical margins can only be given by postoperative pathological examination of the surgical specimen after resection. After surgery, the margins of resected tissues are examined by a pathologist to determine whether or not the surgical specimen has clean margins. If a positive margin is detected, the patient might need additional surgery or therapy. If it would be possible to detect tumour margins more accurately during surgery, tumour resection could be improved.

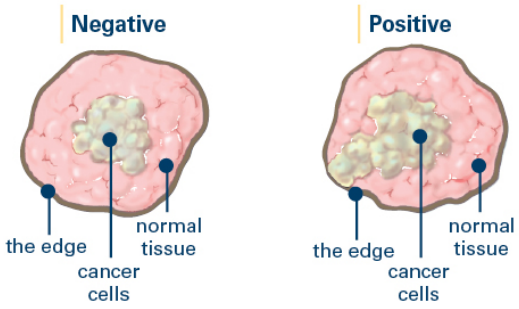

Figure 1.1: Circumferential resection margins. Left: a negative margin, no tumour is present on the edge. Right: a right positive resection margins, tumour tissue is present in the edge [6].

1.1.2 Fluorescence-guided surgery

Near-infrared molecular fluorescence guided surgery (NIR-MFGS) is a combination of optical molecular imaging using near-infrared light (NIR-MFGS) and tumour specific fluorescent tracers and is a promising technique to improve cancer detection. Molecular imaging provides the visualization, characterization and measurement of biological processes at the molecular and cellular level. NIR-MFGS gives an opportunity to visualize tumours and tumour margins in vivo in real time, providing a guiding technique for oncology surgeons to reach improved radical resection. Additionally, it does not alter the surgical field of view, has low costs and high flexibility. A limitation is the penetration depth at around 1 cm, so only superficial activity can be detected with a high sensitivity [7]. Furthermore, a dedicated camera system is required to detect the fluorescence, as the human eye is not sensitive for the NIR light.

A NIR-MFGS system is currently explored in the University Medical Centre Groningen (UMCG). This system is based on a near infrared laser (760 nm), and the fluorescent tracer (Bevacizumab-800CW). The tracer consists of an antibody (Bevacizumab), which binds to a tumour specific molecule (VEGF-A), and a fluorescent part (IRDye800CW). VEGF is targeted as it participates in tumour angiogenesis and is responsible for tumour metastasis and prognosis, enhances vascular permeability and is reported to be over-expressed in tumour lesions compared to normal tissue [8, 9]. The fluorescent part is excited by the near-infrared (NIR) light and the reflected light is captured by a camera. IRDye800CW has excitation/emission maxima at 774 nm/789 nm. Together, the intraoperative system and tracer make it possible to visualise a tumour in real-time during surgery.

Although NIR-MFGS is a promising technique, capturing the intrinsic fluorescence signal in a quantifiable way is still difficult. At this moment, the measured fluorescence cannot be quantified as no absolute measurements can be obtained and optical properties cannot be measured simultaneously. Fluorescence is often visualized by scaling it to the maximum intensity in the image or by a pre-defined threshold window. This limits comparison between images and especially comparison between different patients.

1.2 Technical background

1.2.1 Light

The 'light' part of the electromagnetic spectrum ranges from ultraviolet ($<$ 400 nm), to near-infrared light ($>$ 700 nm) with the visible spectrum ranging from 400 - 700 nm. Light can be described with both an electromagnetic wave model (classical wave theory) and a particle model (quantum theory). The first model describes the aspects related to the propagation of light, and thus the interaction of light with different media. These interactions can result in scattering of light. The second model is based on photons carrying energy and interacting with other particles. This explains the increase and decrease in energy observed in phenomena like absorption and fluorescence. The two models are related as an increase in wavelength, causes a decrease in photon energy:

$$E = hv \tag{1.1}$$

where E is the photon energy, h is Planck's constant and v is the frequency of the wave.

Light that encounters tissue will follow one of three possibilities: (1) the light is directly returned towards the source (reflection), or is either (2) absorbed within the tissue (absorption) or (3) transmitted in another direction (scattering) and then back to the source. The interaction of light with any material is dependent upon the properties of incident light and optical properties of the material. The properties are tissue specific and wavelength dependent. Where absorption is the result of energy uptake by matter, reflection and scattering are both due to variations in the refractive index of different tissues. In turbid media, and specifically in the NIR spectral region, light scattering is the dominant process and limits the optical penetration depth [10].

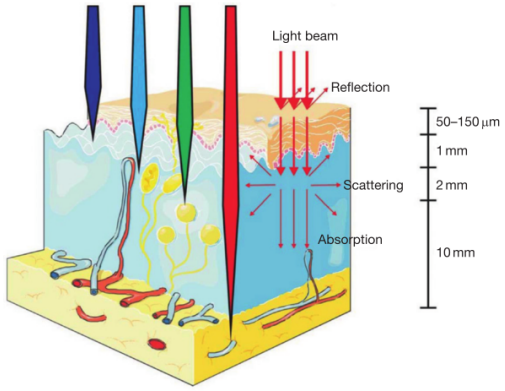

Figure 1.2: Propagation of light through tissue depending on wavelength and tissue interaction (reflection, scattering & absorption) [11].

1.2.1.1 Scattering

Scattering is induced by variations in the refractive index of two media which causes a bending of the light (refraction) and therefore a change in direction. The refractive index for a medium determines the speed of light in the medium and is described as the ratio of the speed of light in a vacuum (c) to the speed of light in that material (v):

$$n = \frac{c}{v} \tag{1.2}$$

Tissue components influence the refractive index, therefore, refractive indices are tissue dependent When light encounters a change in the refractive index, this can evoke both scattering and reflection

of the light. The amount of light reflected by and transmitted through a boundary depends on the refractive indices (n) of the two materials, the angle of incidence (θ), and the polarization of the incoming light [12].

Loss of direction causes a limited penetration depth and blurring of the light, leading to a decrease in accuracy of the localization of the light and strength of the measured signal. On the other hand, highly scattering tissue can increase the chance for an interaction and can therefore increase the measured fluorescence intensity. The net effect of the scattering depends on the exact optical properties of the tissue [13, 14].

An example of scatterers are erythrocytes in blood, elastin and collagen. As erythrocytes are scatterers, the scattering properties of blood are dependent on the haematocrit. The reason for the scattering of both elastin and collagen are the small-scale inhomogeneity's and the substantial variation they form in structures [15, 16].

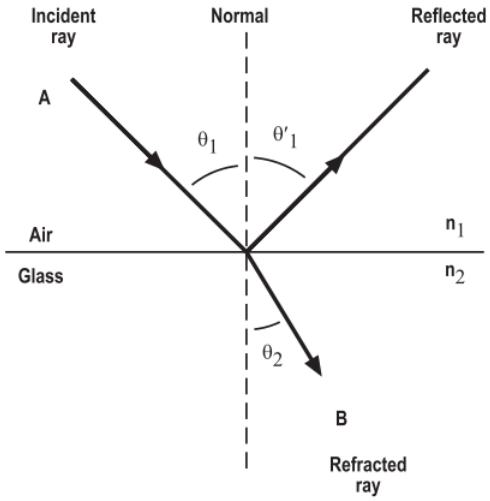

Figure 1.3: Refraction: where n_1 and n_2 are the refractive index for medium 1 and medium 2, respectively. θ_1 is the incident angle, θ_1' the reflected angle and θ_2 the refracted angle, both with respect to the normal [12].

The average amount of scattering is quantified by the scattering coefficient μ_s, which describes the probability of scattering for each photon per unit pathlength:

$$\mu_s(\lambda) = \sigma_s(\lambda)\rho_N \tag{1.3}$$

However, photons can have a high scattering coefficient, but also exhibit high forward scattering. This results in a more moderate loss of the light in the direction of propagation. The reduced scattering coefficient accounts for the influence of the scattering angle or anisotropy (g). The anisotropy is a measure for the amount of forward directed scattering and lies between -1 and 1, where 1 is forward scattering and 0 is isotropic scattering.

$$\mu_s' = \mu_s(1 - g) \tag{1.4}$$

Reflection Reflection is the most extreme form of scatter where the photon does not even penetrate tissue. For reflected light, the angle of incidence θ_1 on a tissue is equal to the angle of reflection θ_2 (figure 1.3). Depending on the encountered tissue, reflected light can be divided into three types: specular, spread and diffuse reflection. Specular reflection occurs on polished, mirror-like surfaces, where the

angle of incidence is (almost) identical to the angle of refraction. This type of reflections can interfere with a desired signal, as it generates a strong signal, but contains no information about the underlying tissue. A cross-polarization filter could solve this problem and block the specular reflection. Diffuse reflections occur when a rough or matte surface reflects the incident light at many different reflection angles. The spread reflections occur because an uneven surface reflects light at more than one angle, as the reflected angles are all the same as the local incident angle which varies over the surface [12, 17].

The reflectance signal can correct fluorescence images for differences in geometry and distance to the tissue and to quantify results, as reflectance can detect local changes in optical properties of tissue and illumination [18, 19].

1.2.1.2 Absorption

Absorption is the attenuation of light and is tissue-specific. Molecules within the tissue absorb photons when the photon's energy matches an interval between internal energy states. The absorption of energy causes the molecule to go from a ground state to an excited state. The release of this energy by the molecule is called decay and is accompanied by the release of heat or the emission of a photon, resulting in fluorescence. Due to the attenuation, light loses its energy and therefore its penetration depth decreases. The absorption is quantified by the absorption coefficient which represents the inverse mean path length of a photon before absorption:

$$\mu_a(\lambda) = \sigma_a(\lambda)\rho_N \tag{1.5}$$

The higher the absorption coefficient (μ_a), the higher the probability that a photon is absorbed.

The main absorber in tissue is haemoglobin, in both the oxygenated and the deoxygenated state, it accounts for 39-64% of the total light absorption (figure 1.4) [20]. Especially in the visible window the absorption of haemoglobin is high. With an increase in wavelength, the absorption is decreasing. However, at longer wavelengths, the absorption of water becomes dominant. Also in the short wavelengths region water contributes significantly to the attenuation because its concentration is very high in biological tissue [15].

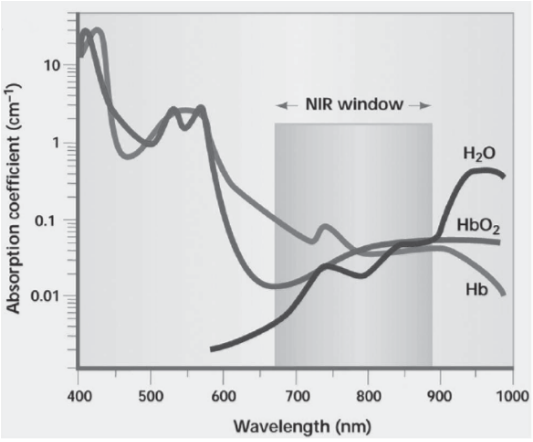

Figure 1.4: Absorption coefficient of oxygenated and deoxygenated haemoglobin and water for different wavelengths. The absorption coefficient for the Hb and water combined is the lowest in the NIR window [21].

1.2.1.3 Fluorescence

Fluorescence is a special absorption phenomenon, where light photons are absorbed by a medium (excitation) and released with a longer wavelength (emission). This change in wavelength is caused by a decrease in energy, due to generation of heat and is called Stokes shift. This phenomenon can be visualized with a Jablonski diagram (figure 1.5)

To decrease the influence of absorption and scattering, NIR light is used instead of visible light to excite the fluorophores. The NIR spectrum has the additional benefit to reduce autofluorescence resulting in an increased tumour-to-background ratio and improve penetration depth.

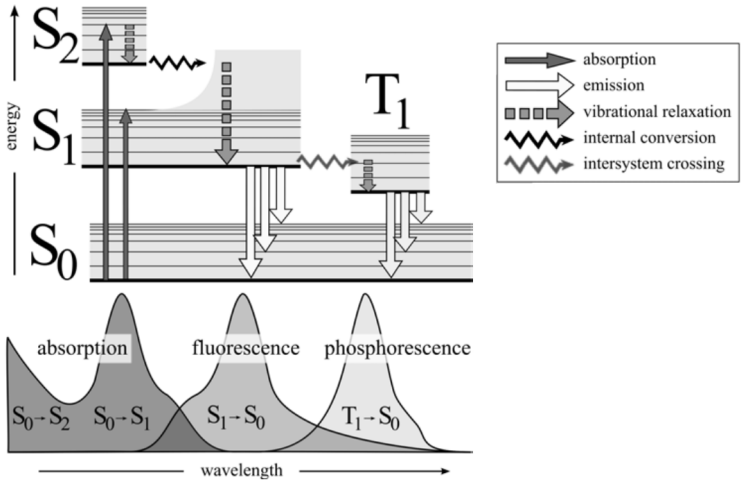

Figure 1.5: Jablonski diagram. The diagram consists of three electronic stages, ground (S_0), first (S_1) and second (S_2) electronic stage. At each of these electronic levels the fluorophores can exist in several vibrational energy levels (thin lines). The absorption of light by a fluorophore raises the energy level to an unstable excited state (S_1 or S_2), also known as excitation. The excitation is characterised by a very short half-life (1-10 nanoseconds), during this period, the fluorophore generally relaxes toward the lowest vibrational energy level within the electronic excited state. The energy lost during this process is released as heat [22].

1.2.2 Quantification

The fluorescence intensity is influenced by multiple factors and these must be accounted for when quantifying fluorescence. First, as mentioned before, the optical properties not only influence the intensity of the measured signal, but also its spatial distribution. More absorption results in less signal and more scattering causes more signal, but alters the distribution as well.

Second, measurement settings influence the detected fluorescence. Differences in illumination, distance and angle of source to tissue and exposure time causes changes in the detected fluorescence. Uneven illumination of the specimen results in an uneven fluorescence signal, even if the concentration is equal, as the illumination intensity is proportional to the fluorescence emission. Additionally, an increase in exposure time, the time the specimen is exposed to light, increases the measured fluorescence signal. Underexposure can lead to a weak signal and overexposure can cause saturation of the pixel intensity and therefore an inaccurate quantification. Saturation is when the detection capacity of the photon detectors is reached. An increase in photons will no longer result in an increase in fluorescence signal. Importantly, fluorescence sources close to the surface contribute much more to the signal than more deeply embedded ones.

Third, the camera system also causes differences in measured fluorescence. The camera generates a dark current, which is the signal measured without any light source on. Furthermore, the system will always induce a form of noise to the signal. Noise causes variance in the intensity values above and below the 'real' intensity value of the signal. The extent of deviation differs per pixel. Noise causes imprecision in measurements of pixel intensity values, and therefore a level of uncertainty in the accuracy of the measurement. Finally, not only the tumour binds the fluorescent tracer, the background can sometimes do this as well. This could result in high background signals, making it more difficult to distinguish between tumour and background. Additionally, some tissues are fluorescent even without the presence of a fluorophore.

Without correction for these factors, observed differences between strong and weak fluorescence intensities can be the result of the concentration, optical properties and/or system properties. Furthermore, comparison between multiple images is difficult. To apply fluorescence guided optical imaging clinically and therefore have a clear distinction between tumorous and non-tumorous tissue, objective detection and measurement of the fluorescence signal is necessary. Ultimately, obtaining the intrinsic fluorescence, which is the fluorescence without the influence of the optical properties, including measurements differences and system properties would be desirable. The goal would be to compare between patients and have a general intensity scale for fluorescent tumorous tissue, resulting in a clear differentiation between tumorous and non-tumorous tissue.

Currently, different techniques have been developed to compensate for the effect of optical properties [16]. Significant attention has been directed towards quantifying the true fluorescence concentration by correcting for the influence of optical properties on the measured intensity. These techniques can be divided into spatial frequency, spectroscopy and ratiometric techniques. Although multiple studies tried to correct the fluorescence signal, an ultimate solution is not available yet.

Spatial frequency domain imaging (SFDI) relies on projecting a pattern (of sinusoidal fringes) onto tissue at different spatial frequencies and phases and then measuring the resulting reflectance. From the reflectance image, the tissue modulation transfer function (MTF) is extracted at every location, which is the Fourier equivalent to the point spread function. As the reflection of the tissue is different at each wavelength, the correction can be measured [23–28]. Ratiometric methods are based on the use of a ratio between two measured intensities. For fluorescence, often the fluorescence-reflectance ratio is used to account for the optical properties and differences in illumination. These methods can be performed with one or multiple excitation and emission wavelengths. The multiple wavelength approach can also correct for the autofluorescence, which is not possible with the single wavelength approach. These approaches were shown to be beneficial for correcting differences in irradiance and absorption, however, a crucial limitation of ratiometric methods is that they are performed on a pixel-by-pixel basis and they do not model the interaction of neighbouring regions. An advantage of ratiometric techniques is their ease of implementation, limited assumptions, and limited computational power requirements.

1.3 Aim of this study

Fluorescence guided surgery is a promising technique, but is complicated by the fact that it is difficult to obtain the intrinsic fluorescence signal. The clinical challenge is to improve the differentiation between tumorous and non-tumorous tissue and make it absolute.

In this research, two imaging systems are used for fluorescence imaging: a black box and an intra-operative camera. The black box acquires a white light (RGB) image and a fluorescence and excitation image at a wavelength of 760 nm. For the intraoperative system, no excitation image is available, instead the red channel of the white light could be used. Therefore, the difference between the correction with the excitation image or red channel image should be determined. Furthermore, as no satisfying correction method is available yet, two methods will be compared for the correction of fluorescent images.

The aim of this study is to improve quantification of the fluorescence signal measured in surgical specimen to acquire a more objective observation of the fluorescence intensity measured and ultimately, make a clear distinction between tumorous and non-tumorous tissue based on an absolute colorscale. The final results will be compared to the golden standard of histopathological examination.

1.3.1 Objectives

1.3.1.1 Primary objective

The primary objective of this study is to determine the feasibility of quantification of fluorescence, to distinguish tumorous from non-tumorous tissue, by correcting the fluorescence signal for influences of illumination differences and tissue optical properties.

1.3.1.2 Secondary objectives

1. Compare the effect of the red channel image and excitation image on the correction of the fluorescence signal
2. Calculate the difference in the correction of the fluorescence signal between the black box and intraoperative camera
3. Identify the difference in performance of the correction method for both a phantom and real tissue data.
4. Identify possible optimisation steps for improving fluorescence imaging acquisition.

2 | Validation of the ratiometric correction method with a 3D printed phantom

2.1 Introduction

Differentiation between tumorous and non-tumorous tissue is crucial in fluorescence imaging. Currently, differentiation and thus quantification of the fluorescence signal is complicated by multiple factors like the influence of optical properties, measurement variations and imaging device settings. The optical properties consist of the scattering and absorption coefficient and differ per tissue type. Absorption causes light attenuation and scattering leads to a difference in both the light intensity and spatial distribution. In tissue, and specifically in the NIR region, light scattering is the dominant process of the two. The effect of scattering on the spatial distribution is of particular importance for the accurate delineation of tumour margins in surgical imaging. Furthermore, measurement settings like gain and exposure time influence the measured fluorescence intensity, making it difficult to compare fluorescence intensity signals with different settings. Finally, each imaging device has its own illumination settings and resolution influencing the measured fluorescence intensity. Implementation of fluorescence imaging in a clinical setting requires objective measurements of the fluorescence intensity and a high accuracy in tumour visualisation and quantification.

Significant attention has been directed toward quantifying the intrinsic fluorescence intensity. To acquire the intrinsic fluorescence signal, the signal must be independent of tissue optical properties, illumination variations (angle/distance) and exposure time. Multiple approaches have been used to quantify fluorescence (see 1.2.2). Some methods use transillumination, tomography, hyperspectral imaging or spatial frequency domain techniques to acquire more information about the optical properties of the tissue to correct the fluorescence diffusion [19, 23, 28, 29]. In our study we are limited to the fluorescence imaging systems already used in the clinic and these do not provide the information for the before mentioned methods. The fluorescence imaging system only allowed for single wavelength correction methods. Single wavelength ratiometric correction method is an option and is applied before by multiple researches to correct fluorescence images [18, 29–33]. Here, the excitation or red channel image is applied to correct the fluorescence image. Themelis et al. corrected both the fluorescent and excitation images for the dark current, the signal that is captured by the imaging device without any light source present, and divided the fluorescence image by the excitation image. If the denominator value was below a certain threshold, the resulting value was set to zero to prevent division by low values. As division by low values can result in high intensities in the resulting image.

$$C_{fluo} = \frac{I_{fluo} - D_{fluo}}{(I_{ex} - D_{ex} > T)} \tag{2.1}$$

where C_{fluo} is the corrected fluorescence image, I_{fluo} is the uncorrected fluorescence image, and D_{fluo} is the dark current image, respectively. I_{ex} is the excitation imaging, and D_{ex} is the dark current image corresponding to the excitation settings.

Themelis et al. showed that quantification errors decreased from 25% for uncorrected images to less than 8% for corrected image [32]. Furthermore, Ntziachristos et al. applied the method of Themelis and also found improvement in imaging performance by reducing sensitivity to the effects of optical properties in tissues and for variations in the strength of the illumination field [29].

In our study, we adjust the formula of Themelis et al. and applied it to 3D phantom images. The adjustment includes that if the denominator value comes below a certain value, C_{fluo} is set to the threshold value instead of zero, so that less information is lost within the image. Furthermore, the exposure time and if necessary gain is added to the correction. The total correction is applied to fluorescence images of a 3D phantom made with both a static black box and an intraoperative system. The aim of this study is to validate the correction method, the influence of multiple factors on the fluorescence intensity and to compare the black box and intraoperative camera.

2.2 Method & Materials

2.2.1 Development

Our fluorescence imaging device can acquire fluorescence images at one wavelength (760 nm), simultaneously with an RGB image. Furthermore, a black box is employed for validation of intraoperative specimen images and acquires a fluorescence, excitation and RGB image. To validate our correction method and compare both imaging systems, a 3D phantom will be used for fluorescence imaging. Ideally, our correction method can be applied automatically to all bread loaf slices of one patient and provide (close to) real time correction of these images. Finally, a standard colormap, per tumour type and imaging device, should visualize the difference between tumour and non-tumorous tissue.

Phantom The purpose of the phantom is to validate the developed correction method and to visualize the effect of the correction method with known parameters. The solution should be homogeneous throughout the phantom and fluorescence should not leak into the surrounding solution. Furthermore, the phantom and surrounding should reduce/prevent specular reflections in all images. Last, replication of results should be made possible.

Colormap The colormap should provide standard values for distinguishing tumorous from non-tumorous tissue. These values are based on the excitation corrected images and are defined according to our results. However, the excitation images are affected by the position of the polarizer. Therefore, an optimal position of the cross polarizer, passing only excitation light, is important.

2.2.2 Materials

2.2.2.1 Phantom

A 3D printed phantom was used as validation of the correction method (figure 2.1). This phantom was made of VeroClear (Stratasys RGD810) and consisted of 5 buried cups: located at three different depths (2, 3 and 4 mm) and containing three diameters (2.5, 5 and 7.5 mm) (table 2.1). The total height of the phantom was 5 mm.

First, 200 mg of agar agar was dissolved in 10 ml PBS (phosphate buffered saline) and heated until 90 °C under constant stirring. The liquid agar agar and bevacizumab-800CW were combined and the five cups were filled to contain 0.13 uM each. Next, the phantom was cooled in the refrigerator (4-7 °C) for at least 15 minutes to solidify the agar. Meanwhile, a gelatine solution was made with ink and intralipid to provide for absorption and scattering properties. The higher melting point of agar compared

to gelatine prevented dissolving and leaking of fluorescent dye from the agar to the gelatine when pouring the gelatine into the phantom. The gelatine solution (4 mg gelatine with 40 ml PBS) was heated to 50°C and stirred until dissolved. When fully dissolved, the intralipid (1%) and India ink (1:500) were added. Last, the solution was poured into the phantom and the phantom was cooled in a refrigerator (4-7 °C) for at least 30 minutes until solidified.

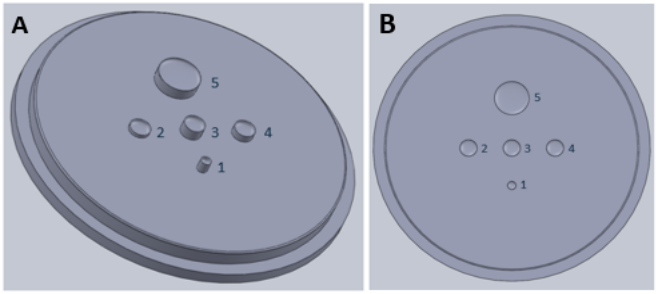

Figure 2.1: A is the angled view and B top view of the 3D printed phantom

Cup	Diameter (mm)	Depth (mm)
1	2.5	4
2	5	2
3	5	4
4	5	3
5	10	4

Table 2.1: The diameter and height per cup

2.2.2.2 Black box

The black box (Surgvision, The Netherlands) consists of four LED lights, a lens, a filter wheel and a digital CMOS camera (figure 4.1). Two of the LED's were used for white-light (400-700 nm) illumination and two for NIR illumination (>700 nm). The two white LED's (gray in figure 4.1) and the two NIR lights (red in figure 2.3) were positioned on diagonally opposite sides above the sample, forming a square with the white-light LED's. The white light LED's were used for acquiring an RGB image (colour registration) and the NIR LED's for acquiring the fluorescence and excitation image. In front of the lens, a polarisation filter is located that can be manually adjusted. This polarisation filter decreases the specular reflections from the surface and was applied for all images. On top of the lens a filter wheel is located. For each image another filter was used. For the RGB image, three filters were applied independently (see table 2.2). So, the red, blue and green images were taken after each other, ultimately creating one RGB image with a fixed exposure time of 40 ms. For the fluorescence image, two filters, a bandpass and longpass filter, were used simultaneously. The NIR LED applied a narrow spectrum (<10nm), peaked at 760 nm. The exposure time of the fluorescence image can be manually adjusted. For the excitation image, no filter is applied, and the image was made with a fixed exposure time of 20 ms. All images are captured with a digital CMOS camera. Finally, the images are viewed and stored on a computer.

Table 2.2: Overview of available filters in the filter wheel of the black box.

Filter	Main wavelength (nm)	Bandwidth (nm)
Blue	450	70
Green	535	50
Red	650	100
Fluorescence LP	>776	-
Fluorescence	819	44
Reflectance	-	-

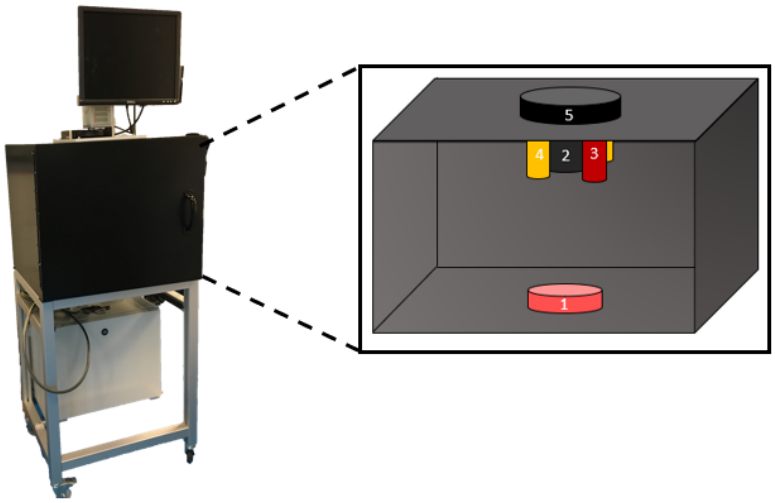

Figure 2.2: Overview of the black box. 1. Bread loaf slice. 2. Camera lens + polarisation filter. 3. NIR LED's 4. RGB LED's 5. Filter wheel.

2.2.2.3 SurgVision Explorer Air

The intraoperative system (SurgVision, The Netherlands) consists of a ring of LED's, motorised lenses, a dichroic mirror, bandpass filters and two cameras' (figure 2.3). The LEDs are divided in a white light LED's and a NIR LED's (excitation wavelength was 760 nm) and alternately positioned on a ring (different from figure 2.3). A dichroic mirror separates the reflected light into white light and NIR light. The white light passes through a polarizer and is captured by a colour camera. The NIR light is filtered by a band pass filter and captured by a single photon detection EMCCD camera. Finally, the images are processed and saved on a computer. A black box (Vault, SurgVision, The Netherlands) for the intraoperative camera was used to provide stable, repeatable measurements.

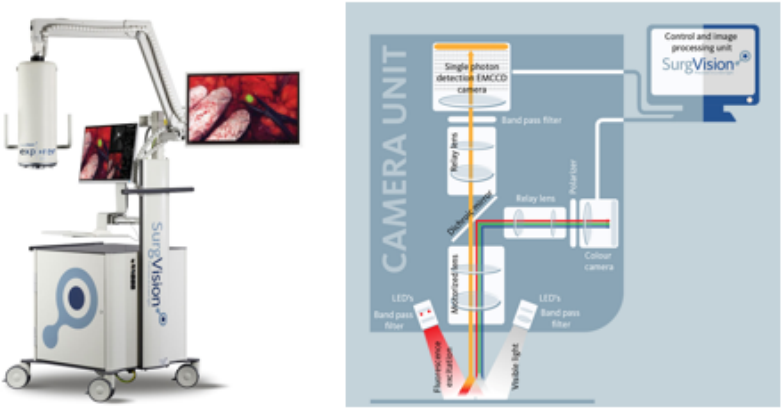

Figure 2.3: Schematic overview of SurgVision Explorer Air system.

Table 2.3: Properties of both the intraoperative camera and black box

	Intra-operative camera	**Black box**
Excitation	760 nm	760 nm
Filters	Dichroic mirror	Semrock FF01-776/LP-25
	Band pass filter 819/44	Semrock FF01-819/44-25
		FF01-450/70-25
		FF01-535/50-25
		FF02-650/100-25
Resolution	30-150 μm	120 μm [1]
Sensitivity	60 picomolar	unknown
Camera	iXon Life 897 EMCCD (Andor Technology)	Hamamatsu Orca-flash4.0 LT
Field of view (FOV)	8.2 x 8.2 cm	10x10 cm
Exposure time	25 ms - 6.4 s	175 ms - 8 sec
Gain	10, 100, 300	-
Working distance	23 cm	cm
Pixel resolution	512x512 (fluorescence)	512x512 (fluorescence)
	1100x1200 (RGB)	2048x2048 (excitation & RGB)
Dynamic range	8 bits	8 bits (fluorescence & RGB)
		16 bits (excitation)
Pixel size	16 μm	6.5 μm
Fill factor	100%	-

[1] Measured manually with 1951 USAF resolution test chart

2.2.3 Theory

The correction technique was divided into three parts: pre-processing, correction and post-processing. The pre-processing part consisted of correction of the images for linear processes like exposure time and gain and adjusting the size of the images. The properties (size and class) of the fluorescence image was used as a reference to which all other images were scaled. This resulted in three images (fluorescence, excitation and red channel) that have the same size (512x512) and class (16 bit) for the black box. Fluorescence images are all set to an exposure time of 1 second and the excitation and red channel image to 0.02 seconds. For the intraoperative camera, two images (fluorescence and RGB) were acquired and scaled to a 512x512 and 16 bit. The correction included the ratiometric correction of the fluorescence image and the post-processing included visualisation of the corrected images.

2.2.3.1 Pre-processing

The acquired images with both the black box and intraoperative camera have their own properties (size, class and exposure time) and needed to be scaled before correction was possible (figure 2.4 and 2.5). First, all images were corrected for the dark current and the image properties. The dark current includes the measured signal in the black box and intraoperative camera without any light source on. These dark current images were acquired for both imaging devices at all possible exposure times.

$$I_{pre-processed} = I_{fluo} - D_{fluo} \tag{2.2}$$

where $I_{pre-processed}$ is the image corrected for the dark current, I_{fluo} is the raw data and D_{fluo} is the dark current image.

The fluorescence image was corrected for the size, class and exposure time. The excitation image and red channel needed to be resized by taken a weighted average of pixels in the nearest 4-by-4 neighbourhood. Furthermore, the red channel needed to be converted to a 16-bit image. As exposure time is assumed to be a linear process, the image could just be divided by the exposure time. Fluorescence images were scaled to an exposure time of one second. The exposure time of the red channel image was equalized to the exposure time of the excitation.

Black box The fluorescence image is binned to 512x512 pixels to acquire a higher sensitivity of the image. Therefore, all other images must also be resized to a 16 bit, 512x512 pixel image. The fluorescence image is only corrected for the dark current image and is scaled to an exposure time of one second.

The excitation image is acquired in 0.02 sec and is a 16 bits, 2048x2048 pixel image. This image is corrected for the dark current image and resized to a 512x512 image.

The red channel image is acquired in 0.04 sec and is an 8 bit, 2048x2048 pixel image. As it is only possible to acquire dark current images at 16 bit, the image is first reclassed to a 16 bits image. Next, it is corrected for the dark current image, the exposure time is equalized to the exposure time of the excitation image and it is resized to a 512x512 image.

Intraoperative camera The intraoperative camera only acquires two images: a fluorescence and a RGB image. The fluorescence image was adjusted for the dark current and the exposure time. The RGB image was also corrected for the dark current and exposure time. Additionally, its size was adjusted from 1100x1100 pixels to 512x512 pixels and scaled to a 16 bit image.

Second, a mask was applied to all three images to set the background to zero. A threshold was used to create a mask from the red channel image and this mask was applied to the fluorescence, excitation and red channel image to set the background pixels to zero. The threshold for the background is set to 0.08. Every pixel below this threshold was stated as background and set to zero. Every pixel above the threshold was left untouched. The masked images were corrected for (isolated) high intensity pixels before the correction could be applied.

Last, isolated, high intensity pixels were replaced by a mean average of surrounding pixels. All images included high intensity pixels due to specular reflections, noise and/or cosmic radiation. These high intensity pixels influence the correction and were removed by first creating a difference map. This difference map was created by first applying a 5-by-5 median filter, which replaces the pixel with the medium value in the 5-by-5 neighbourhood around this pixel. Then, the absolute difference was calculated between the masked image and the filtered image. The difference map was then thresholded. For all images a threshold of 10% of the maximum was taken. For those positions that exceeded the threshold, the mean value of a 9-by-9 window, except for the middle pixel, was calculated and the middle pixels was replaced by the mean value.

Exposure time & gain The fluorescence intensity is measured for multiple exposure times and for the intraoperative camera also for multiple gains. The goal was to show the linearity of the system for both the exposure time and gain.

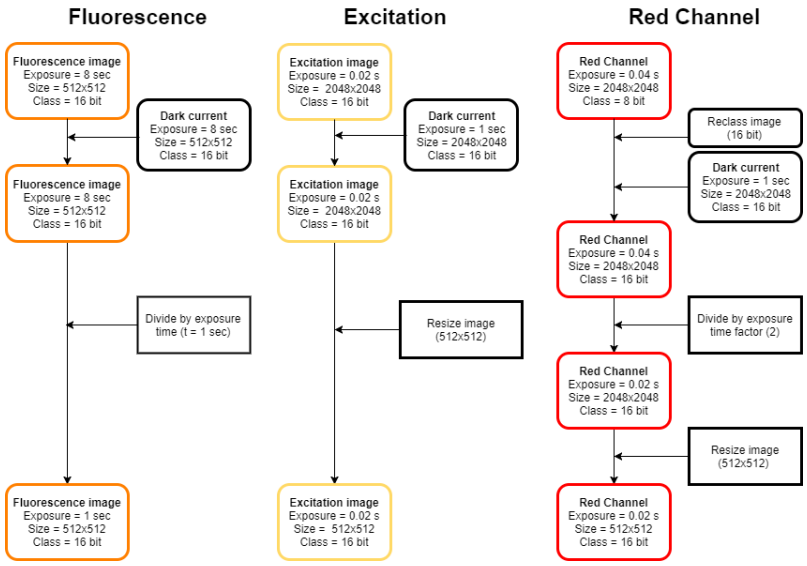

Figure 2.4: Preprocessing of the fluorescence, excitation and red channel image acquired with the black box

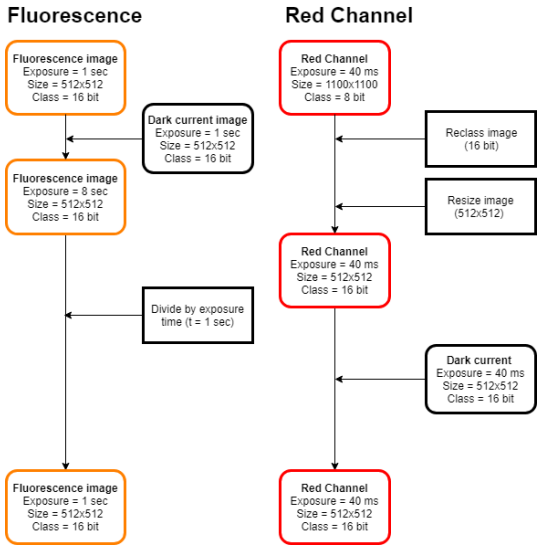

Figure 2.5: Preprocessing of the fluorescence, excitation and red channel image acquired with the intraoperative camera

2.2.3.2 Correction

The correction is based on the correction applied by Themelis et al. [32]. However, where Themelis set the pixels above the threshold to zero, we set them to the threshold value. Therefore, less information is lost and the shape of the phantom is preserved.

$$C_{fluo} = \frac{I_{fluo} - D_{fluo}}{(I_{ex} - D_{ex} > T)} \tag{2.3}$$

where I_{fluo} is the fluorescence image and I_{ex} is the excitation image. D_{fluo} is the dark current image related to the fluorescence filter and D_{ex} the dark current related to the excitation filter. T is the threshold for the excitation image. The threshold is chosen to prevent division by low values, which could result

in high intensities in the corrected image. Themelis et al. applied a threshold of 10% of the maximum value of the excitation image. We studied the effects of multiple thresholds, which will be presented later in this thesis, as the threshold of 10% did not have a sufficient effect in our images.

Comparison The excitation and red channel image will be compared to see if there is a difference in their performance in the correction. As the intensities differ between the excitation and red channel image, a correction factor is calculated. This factor is calculated by measuring the mean intensity (zeros excluded) of the masked pre-processed image in both the excitation and red channel image. The difference in mean value of both images is calculated and the excitation image is multiplied by this factor. The factor was found to depend on the setting of the polarization filter and therefore differed per measurement, due to the manual adjustment of the polarisation filter.

2.2.3.3 Post-processing

In the post-processing step a custom colormap is applied to the images to show the difference between tumorous and non-tumorous tissue. Images made with the same imaging device will be visualized with the same custom colormap. The threshold for the colormap will be defined according to the corrected fluorescence images.

2.2.4 Analysis

The tumour-to-background ratio (TBR), signal-to-noise ratio (SNR) and contrast-to-noise ratio (CNR) will be calculated and compared between uncorrected and corrected image. The contrast-to-noise is an object size-independent measure of the signal level in the presence of noise, where the SNR is dependent on the shape and size of the object. Figure 2.6 shows the chosen regions for the signal and the background for both the black box and intraoperative. The Rose Criterion states that for an SNR $\geq$ 5, an object will almost always be detected ([34]).

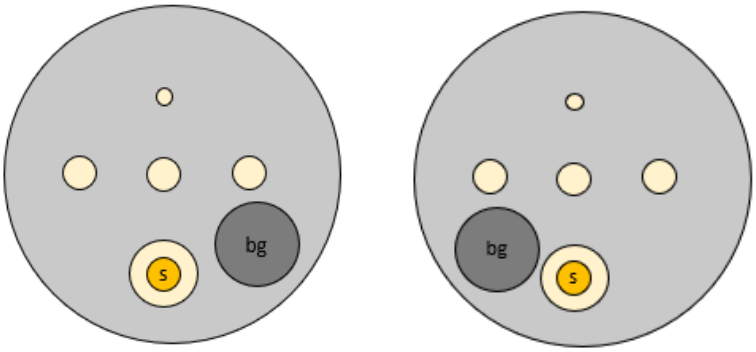

(a) Black box (b) Intraoperative

Figure 2.6: Placement and size of the ROI.

The TBR is the most basic calculation, where the mean value of the tumour ($\bar{x}_t$) region is divided by the mean value of the background region ($\bar{x}_{bg}$):

$$TBR = \frac{\bar{x}_t}{\bar{x}_{bg}} \tag{2.4}$$

The SNR is size and shape of the object dependent. The mean background ($\bar{x}_{bg}$) is subtracted from

each pixel in the tumour region (x_i). All subtracted values are then summed over the tumour region.

$$SNR = \frac{\sum_i (x_i - \bar{x}_{bg})}{\sigma_{bg}} \tag{2.5}$$

The SNR allows for acquiring a non-homogeneous signal region. However, the background does need to be homogeneous and representative for the entire object.
The CNR is a size-independent measure of the signal level in the presence of noise. The mean value in the tumour region ($\bar{x}_t$) is subtracted by the mean value in the background region ($\bar{x}_{bg}$) and ultimately divided by the standard deviation within the background region (σ_{bg})

$$CNR = \frac{\bar{x}_t - \bar{x}_{bg}}{\sigma_{bg}} \tag{2.6}$$

2.3 Results

2.3.1 Black box

2.3.1.1 Preprocessing

Exposure time The exposure time was correlated to the measured mean intensity in a predefined region-of-interest (ROI) (figure 2.7). The same ROI was applied to both the uncorrected and corrected images. Graph 2.8a shows the effect of the exposure time on the measured intensity for both the uncorrected and corrected fluorescence image. Both images show a linear increase in intensity for an increase in exposure time. Graph 2.8b shows the same results, but then zoomed in on the exposure time from 75 to 1000 ms. Even in the lower exposure times, both lines show linearity, although the linearity decreases a little for the lowest exposure times. Furthermore, both graphs showed that an exposure time of zero is more correlated to zero pixel intensity in the fluorescence corrected image compared to the fluorescence uncorrected image. Overall, both graphs showed that the exposure time was linear with the pixel intensity.

When dividing the intensity values for the exposure time, expected was a straight line, especially for the corrected fluorescence image. For the longer exposure times (>1 second), the line is close to horizontal (figure 2.8c). However, for short exposure times (<1 second) the uncorrected image showed a strong increase in signal (from $\pm$0.5 to $\pm$0.35), close to an exponential increase, and the corrected image a small decrease (from $\pm$0.01 to $\pm$0.015) in signal (graph 2.8d). The non-linearity in the shorter exposure times could be a result of a difference in signal-to-noise ratio. For shorter exposure times, the noise signal is more dominantly present. As noise is not linear, correction of these images results in aberrant values.

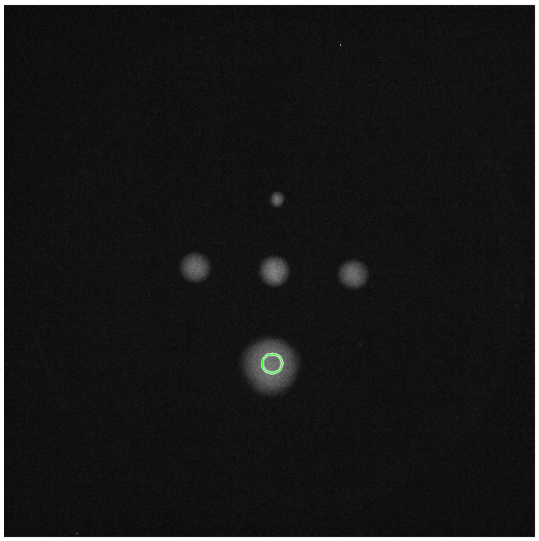

Figure 2.7: Placement and size of the ROI.

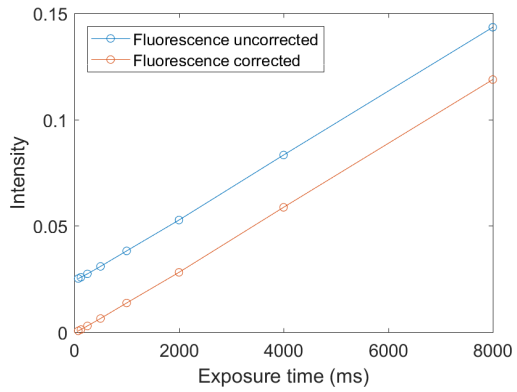

(a) Exposure time versus intensity (75 - 8000 ms)

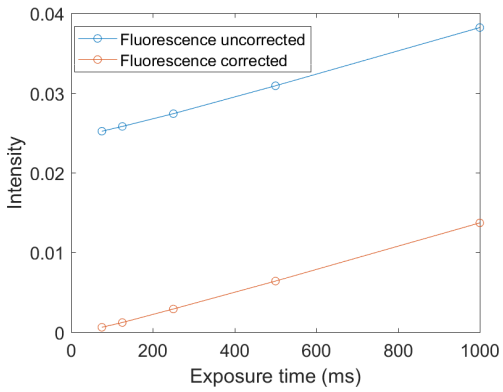

(b) Exposure time versus intensity (75 - 1000 ms)

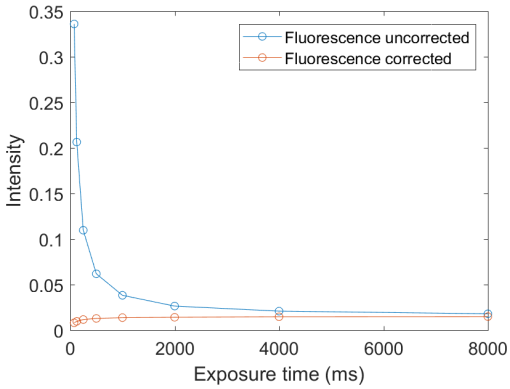

(c) Fluorescence intensity divided by the exposure time

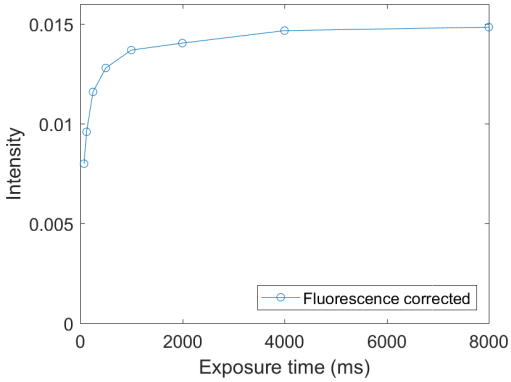

(d) Zoomed in on the corrected fluorescence intensity divided by the exposure time (orange in figure 2.8c)

Figure 2.8: Effect of the exposure time on the intensity in the selected ROI for both the uncorrected and corrected fluorescence image

2.3.1.2 Correction method

Fluorescence intensity The 3D phantom was imaged with only the fluorescence-agar solution, thus, without the gelatine solution, to show the distribution of the bevacizumab-800CW/agar agar solution within the cups. All cups should show equal fluorescence intensity, to secure accurate measurements.

Figure 2.9 shows the uncorrected intensity for the 5 phantom cups. These cups are only corrected for the dark current. The horizontal line, crossing the cups at different depths, shows a little difference in intensity between the three cups. The middle cup showed an intensity of 0.0159 compared to 0.0144 (left) and 0.0139 (right). This effect is also visible for the vertical line. Here, also the middle cup shows a little more intensity, 0.017 compared to 0.0134 (left) and 0.0154 (right).

Effect threshold correction The applied correction method includes a threshold which is a percentage of the maximum value and which is used to prevent division by low values in badly illuminated regions.

Figure 2.10 and 2.11 show the effect of four percentages on the corrected images with the excitation and red channel, respectively. The upper row shows the fluorescence corrected images and the lower row the pixels that would be adjusted to the threshold value. The mean percentage shows the percentage of pixels that will be adjusted according to the applied threshold. The mean adjusted percentage of

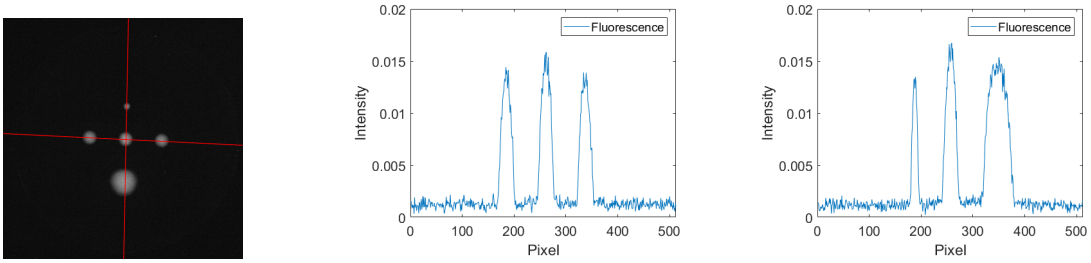

(a) Position of horizontal and vertical line.

(b) Intensity measurement for the horizontal line

(c) Intensity measurement for the vertical line

Figure 2.9: Intensity in 3D phantom without gelatine added. The image is made with an exposure time of one second and only corrected for the dark current.

adjusted pixels (due to under illumination) increases with an increase in percentage, but stay below the 10% for the red channel corrected fluorescence image. Figure 2.10, correction with the excitation image, shows a quick increase in mean percentage of pixels that is adjusted, from 6.93 at 10% to 90.33 at 20%. This quick increase, showed the higher uniformity of intensity values present in the excitation image compared to the red channel image. Due to the difference between the images, two separate thresholds are chosen for the excitation (10%) and red channel image (40%). Resulting in a mean adjusted percentage around 7% for both images. Although the percentages are different, their mean percentage of adjusted pixels are now comparable.

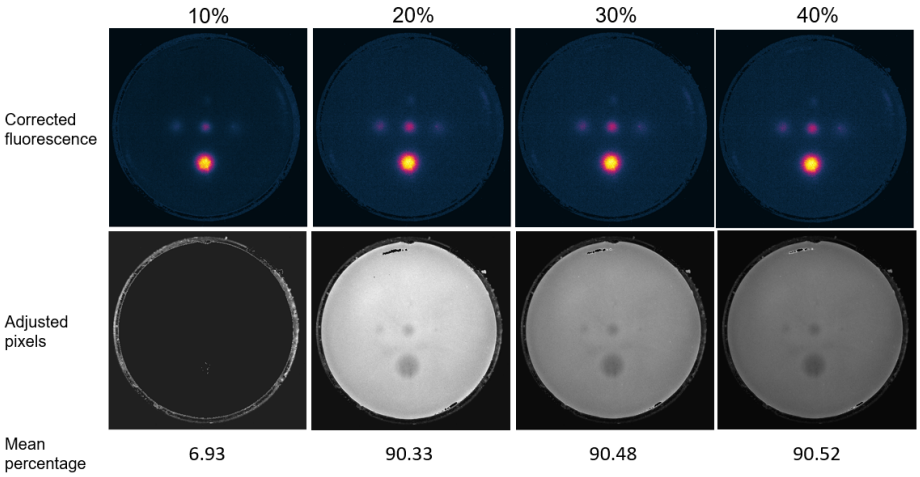

Figure 2.10: Effect of threshold correction on the mean percentage of pixels that are adjusted for the excitation image.

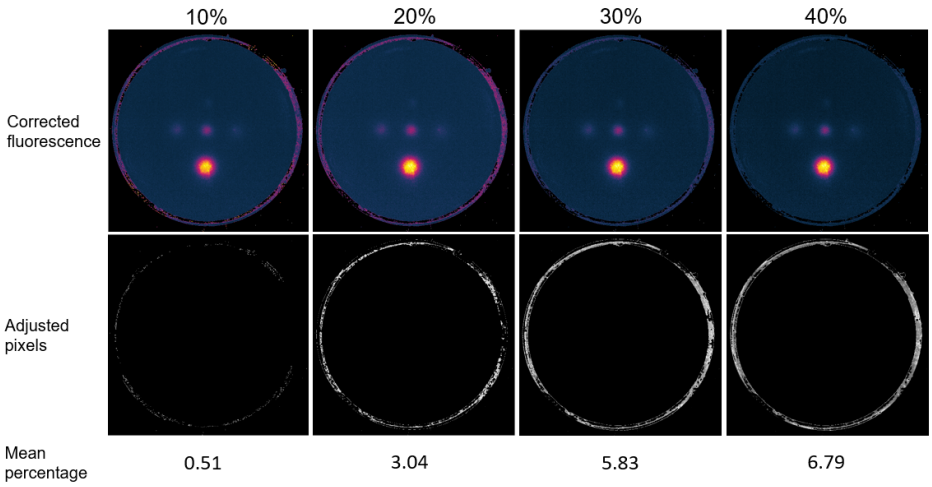

Figure 2.11: Effect of threshold correction on the mean percentage of pixels that are adjusted for the red channel.

Excitation vs. Red Channel Figure 2.12 shows the position of both the horizontal and vertical line for the intensity measurements in the cups. Figure 2.13 shows the intensity-versus-pixel graphs for the horizontal line, thus the difference in cup depth. The top three images (a-c) show the intensity versus pixel for the fluorescence (uncorrected), excitation and red channel image, respectively. In figure 2.13a the effect of the depth of the three cups is clearly visible. The deeper the cup is, the lower the measured fluorescence intensity. Both the excitation and red channel show a decreased intensity were cup 2 (left) and 3 (middle) are located. Cup 4 (right) is too deep to influence these intensity images. Furthermore, the range differs strongly between the excitation image (0 - 0.003) and red channel image (0 - 0.5). The bottom three images show the fluorescence image corrected for both the excitation and red channel and the combination of the corrected images with the uncorrected fluorescence. Both corrected images, show an increase in ratio between the middle cup and the two cups on the side (table 2.4).

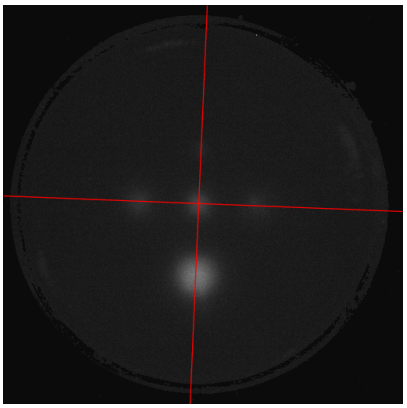

Figure 2.12: Position of vertical and horizontal line for intensity measurements

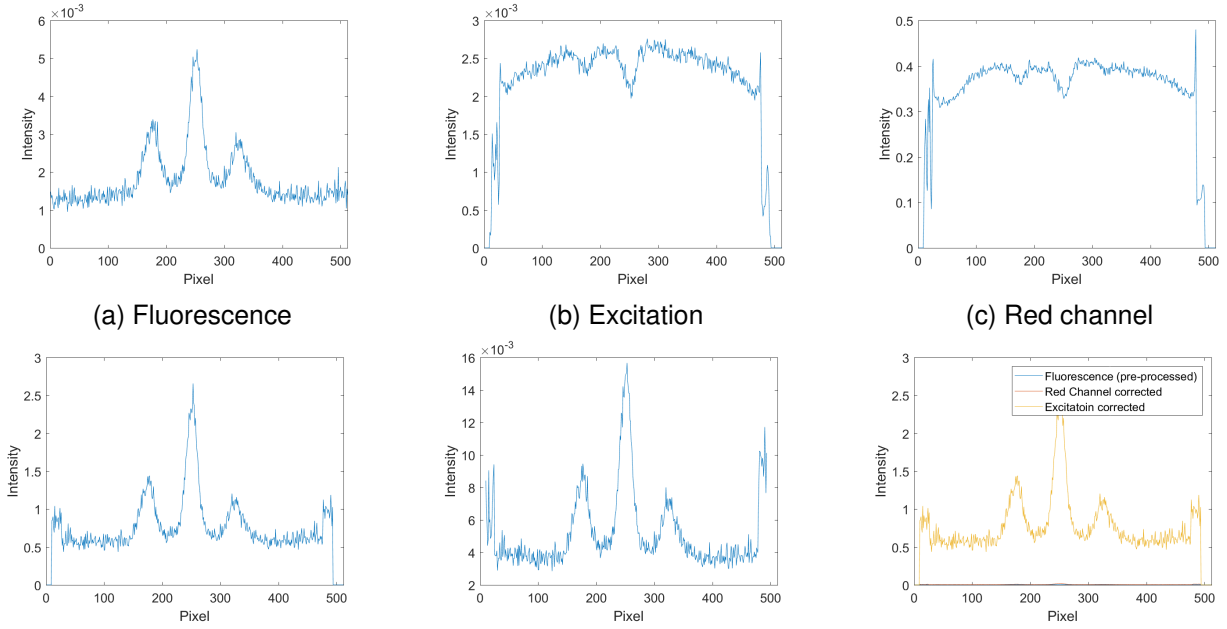

(a) Fluorescence (b) Excitation (c) Red channel

(d) Excitation corrected fluorescence (e) Red channel corrected fluorescence (f) Both corrected images and the fluorescence image

Figure 2.13: The intensity-versus-pixel images for the horizontal line, thus cups with a different depth. Figure A-C show the intensity for the fluorescence, excitation and red channel image. Figure D-F excitation corrected and red channel corrected fluorescent images and the combination of both corrected images and the uncorrected image.

Table 2.4: Ratios over the horizontal line

Image	Cup			Ratio	
	1	2	4	1	2
Fluorescence uncorrected	0.003393	0.00524	0.002874	1.54	1.82
Excitation corrected fluorescence	1.426	2.658	1.158	1.86	2.30
Red channel corrected fluorescence	0.00946	0.01566	0.007296	1.66	2.15

Figure 2.14 shows the intensity-versus-pixel graph for the vertical line, thus the difference in cup diameter. Again, the top three images (a-c) show the intensity-versus-pixel for the fluorescence, excitation and red channel image, respectively. The middle and left cup show again a decrease in measured intensity. Although, the excitation image shows a higher decrease compared to the red channel. Opposite to the vertical line, both corrected images, show an increase in ratio between the middle cup and the two cups on the side. The ratio decreases between the middle and left cup, but increases between the right and the middle cup for both the correction with the excitation or red channel image (table 2.5).

Table 2.5: Ratios over the vertical line

Image	Cup			Ratio	
	1	2	4	1	2
Fluorescence uncorrected	0.002317	0.005222	0.009047	2.25	0.58
Excitation corrected fluorescence	0.8691	2.507	5.236	2.89	0.48
Red channel corrected fluorescence	0.005392	0.01555	0.03257	2.89	0.47

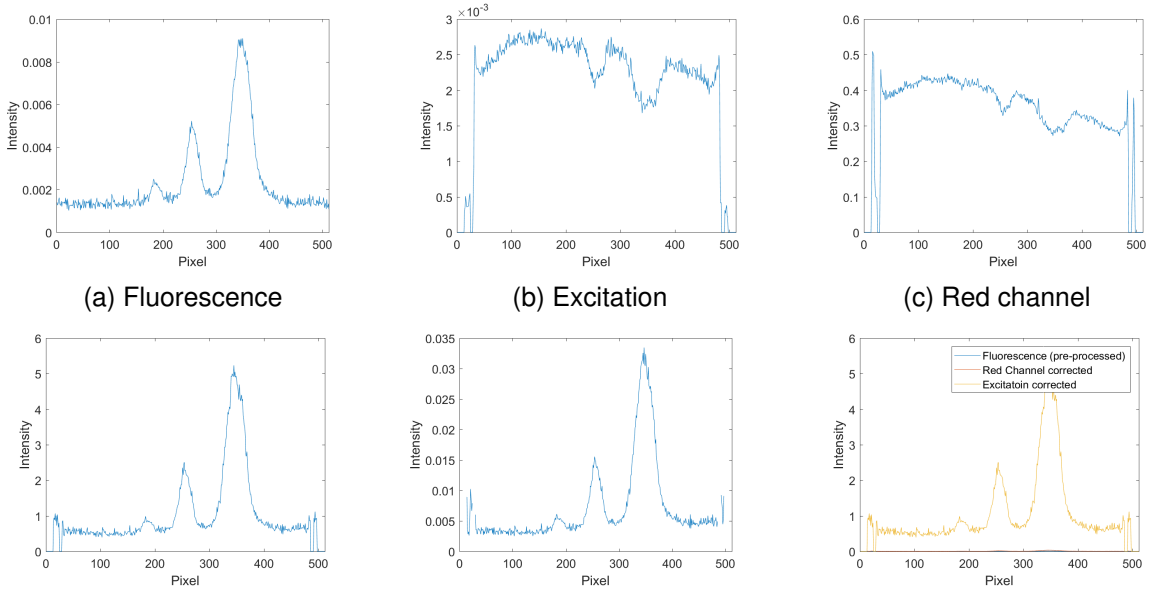

(a) Fluorescence (b) Excitation (c) Red channel

(d) Excitation corrected fluorescence (e) Red channel corrected fluorescence (f) Both corrected images

Figure 2.14: The intensity-versus-pixel images for the vertical line, thus cups with different diameters. Figure A-C show the intensity for the fluorescence, excitation and red channel image. Figure D-F excitation corrected and red channel corrected fluorescent images and the combination of both corrected images and the uncorrected image.

When the red channel is multiplied with the correction factor (1/153), it is shown that the corrected intensities are comparable for both the vertical and horizontal line (figure 2.15).

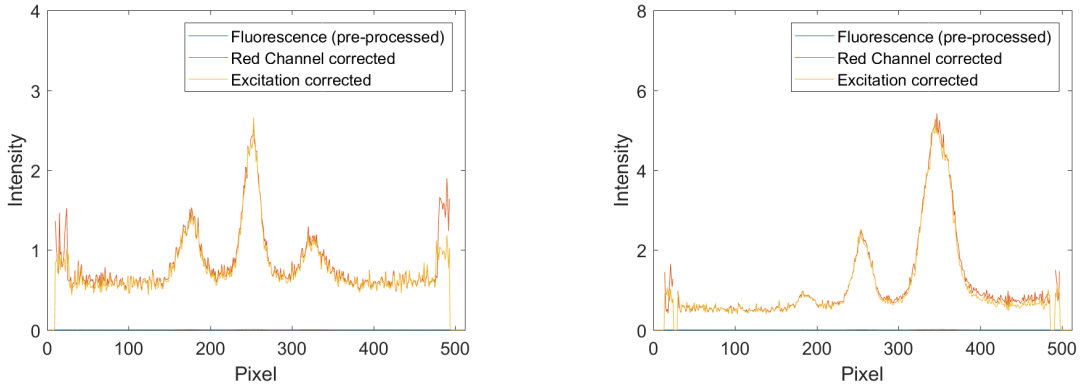

(a) Horizontal (depth) (b) Vertical (diameter)

Figure 2.15: Fluorescence corrected images, where the red channel image is corrected by a factor of (1/153).

2.3.1.3 Post-processing

Colormap The thresholds of the colormap were determined according to figure 2.16. All visible peaks correspond to real fluorescence, furthermore, the intensity of the background (gelatine solution) was equal between both graphs (± 0.45). A trade-off between sensitivity and specificity needs to be made for the determination of the threshold values. Chosen was to show all three 5 cups as tumour. This resulted in a tumour size which was bigger than the cup size. The cups diameter should be around 60 pixels, but when the colormap was applied, the cup was visualized with a diameter of 77 pixels. Both thresholds are close to the base of the peak of the cup with the largest diameter, resulting in including more pixels. The lower threshold was set to 0.65 and the upper threshold to 0.73. Figures 2.17 and 2.18 show only small differences between the different exposure times, but all show the same intensities for the five cups. Four of the five cups are clearly visible, only the cup with the smallest diameter is not clearly visible. Furthermore, all images show high intensities at the border region of the cup. The bottom row shows the effect of the correction and colormap when a manual ROI is drawn to exclude the borders. This has no influence on the visualization of the image. The cups show that the correction does not correct for fluorescence at different depths or different diameters.

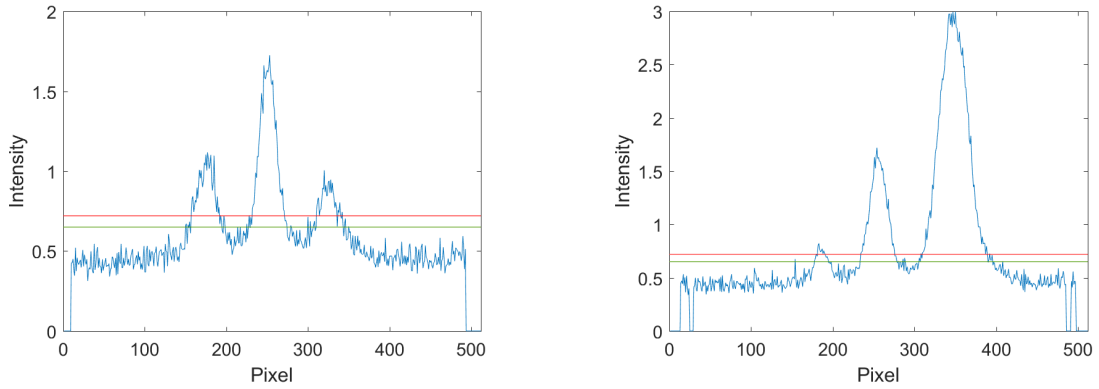

(a) Horizontal (depth)

(b) Vertical (diameter)

Figure 2.16: Intensity-pixel-graph together with the lower and upper threshold of the colormap. Threshold for the colormap.

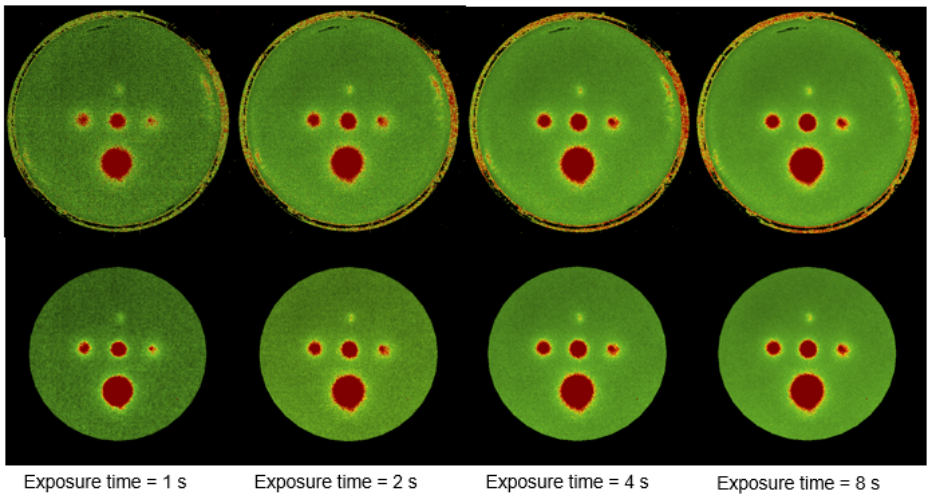

Figure 2.17: Corrected with the reflectance image (threshold 10%)

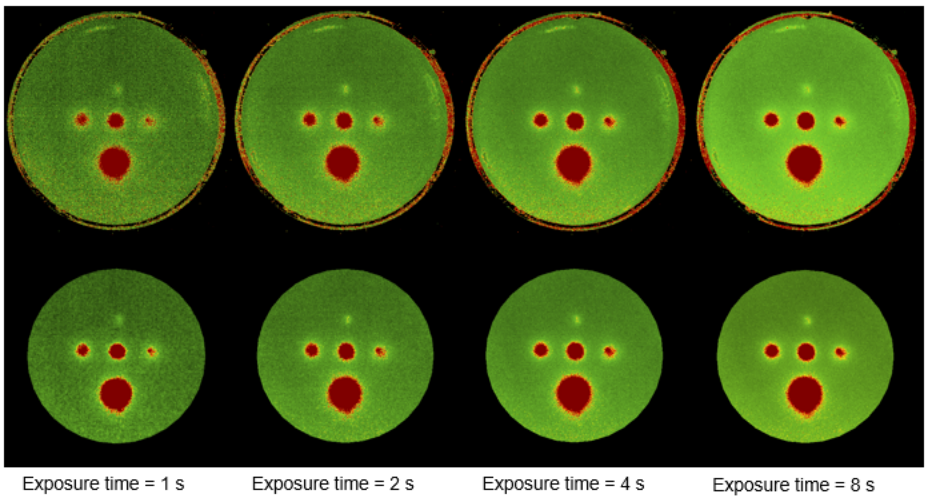

Figure 2.18: Corrected with the red channel (threshold 40%), correction factor (1/153)

2.3.1.4 Analysis

The TBR increases for the uncorrected fluorescence image with an increase in exposure time. Although, this increase is stronger for the higher exposure times. For the corrected images, the TBR decreases for the first four exposure times and increases from an exposure time of 1000 ms and higher. Probably the noise is more dominant in the lower exposure images, causing a decrease in TBR. The SNR and CNR are comparable as our tumour area is chosen within the tumour, without any background. The uncorrected fluorescence image shows an increase of SNR with an increase of exposure time. This response is also visible for both corrected images.

Table 2.6: Overview of the TBR, SNR and CNR for the uncorrected fluorescence images, the excitation corrected fluorescence and red channel corrected fluorescence image.

	TBR			**SNR**			**CNR**		
Exposure time (ms)	Fluorescence uncorrected	Excitation corrected fluorescence	Red channel corrected fluorescence	Fluorescence uncorrected	Excitation corrected fluorescence	Red channel corrected fluorescence	Fluorescence uncorrected	Excitation corrected fluorescence	Red channel corrected fluorescence
75	1.02	-1.24	-1.14	2.43	2.36	1.70	2.43	2.36	1.70
125	1.03	-0.97	-0.84	3.77	2.59	2.04	3.77	2.59	2.04
250	1.06	-0.56	-0.50	7.28	2.87	2.66	7.28	2.87	2.66
500	1.13	-0.76	-0.70	14.08	3.79	3.52	14.08	3.79	3.52
1000	1.27	8.89	8.42	22.97	33.99	25.69	22.97	33.99	25.69
2000	1.48	7.69	7.26	29.49	30.77	35.25	29.49	30.77	35.25
4000	1.90	7.50	7.12	40.11	32.20	48.65	40.11	32.20	48.65
8000	2.54	7.56	7.17	49.42	37.85	59.33	49.42	37.85	59.33

2.3.2 Intraoperative camera

The images used for the correction and calibration of the intraoperative camera were acquired 3 days after making the phantom and thus three days later than the black box images due to logistical reasons. This may have caused a decrease in measured fluorescence intensity.

2.3.2.1 Preprocessing

Exposure time & gain Figure 2.19 shows the intensity versus the exposure time for three gains and for both the pre-processed or uncorrected fluorescence image and the red channel corrected fluorescence image. For the pre-processed, uncorrected fluorescence image, linearity is visible for all three gains until an exposure time of 800 ms. Images with a gain of 300 are saturated above 800 ms, resulting in the loss of linearity. This phenomenon is also visible for a gain of 100, but then from an exposure time of 3200 ms. Images with a gain of 10 show a linear line for all exposure times. For the corrected fluorescence image, the effect of saturation is equal, as it is not possible to correct for this. Furthermore, the corrected images show a much stronger linear relation between the exposure time and the measured intensity. Figure 2.20a shows the intensity versus exposure time, where the images are all scaled to an exposure time of one second. Expected is a straight line for all three gains, where the difference in intensity is only the result of the gain. Again, the effect of the saturated images is visible for both a gain of 100 and 300. The correction the saturated images with the corresponding exposure time results in lower intensities, as it is not a linear process. The fluorescence images with a gain of 10, and thus no saturation, show a straight line as expected. Figure 2.20b the fluorescence images not only corrected for the exposure time, but also for the gain. Expected is one straight line, as the intensities should all match each other. However, as mentioned above, the effect of saturation of the image is visible. For an exposure time until 400 ms the intensities are relatively close to each other. From these graphs it is clear that correct acquisition of the images is very important to avoid saturation, which decreases the linearity of the problem.

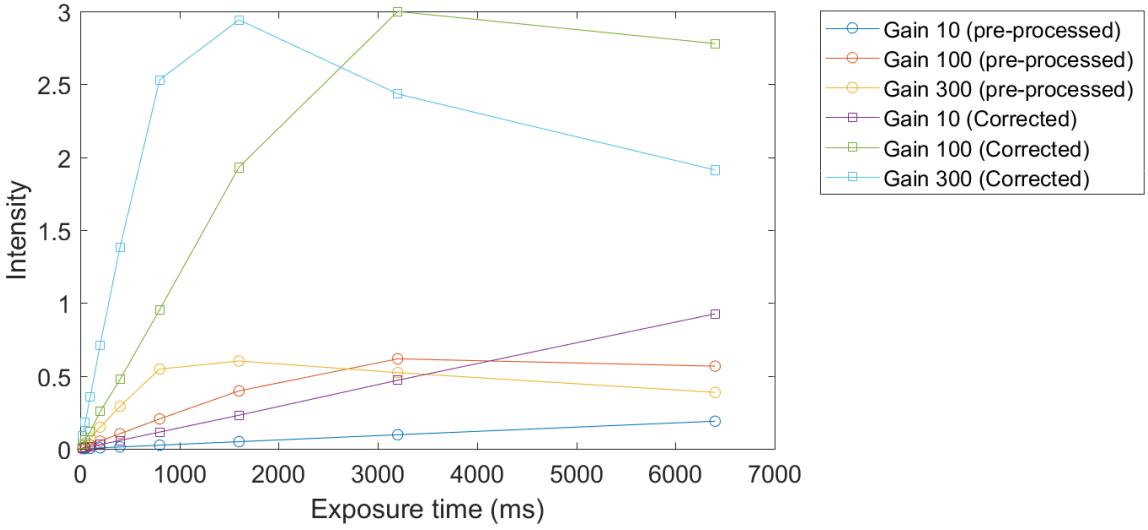

Figure 2.19: Exposure time versus intensity in a ROI measured in the cup with a diameter of 10 mm.

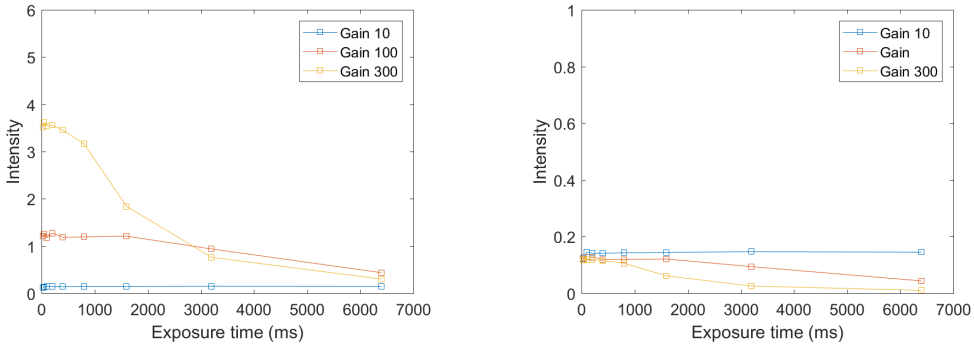

(a) Intensities corrected for exposure time

(b) Intensities corrected for exposure time and gain

Figure 2.20: Exposure time versus the intensity in a ROI measured in the cup with a diameter of 10 mm.

2.3.2.2 Correction method

Intraoperative images could not be corrected directly due to specular reflections in the RGB caused by the white light and excitation laser (figure 2.21a). To still apply our method on intraoperative images, the phantom was positioned that no specular reflections were present around the cups. Next, a manually drawn mask was applied to the fluorescence images to exclude the regions with specular reflections (figure 2.21c and 2.21b).

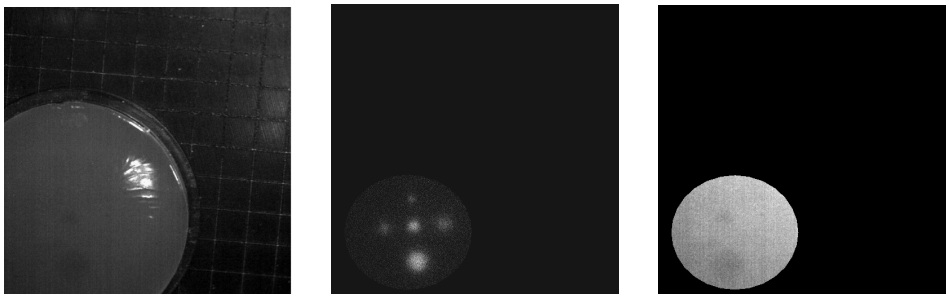

(a) RGB image

(b) Masked fluorescence image

(c) Masked RGB image

Figure 2.21: The effect of the specular reflections on the RGB image (A) and the masked images (C, D).

Equal to black box, the intensity is calculated for the five different cups horizontally and vertically (figure 2.22). Figures 2.22b and 2.22c both show an increase in the ratio between the three peaks for the corrected fluorescence image compared to the uncorrected fluorescence image. Remarkable is the intensity distribution of the red channel in both graphs. The red channel implies that the illumination decreases to the border of the image. Uncorrected, this could influence the measured fluorescence.

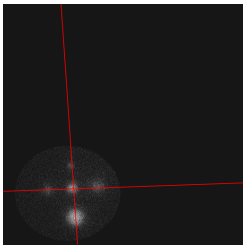

(a) Intensity lines on fluorescence image

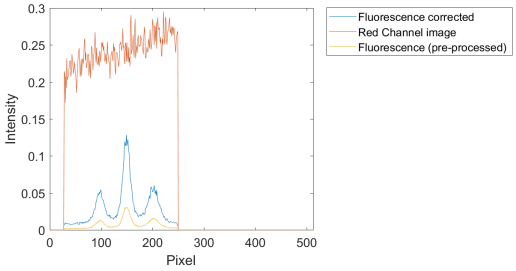

(b) Horizontal (height)

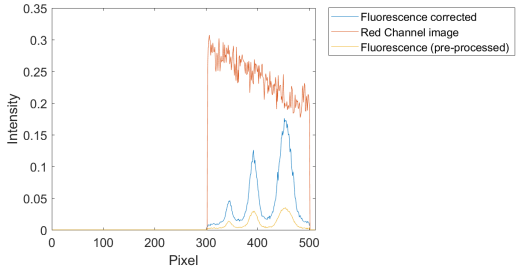

(c) Vertical (diameter)

Figure 2.22: Intensity versus pixel for the fluorescence images corrected with the red channel.

Table 2.7: Effect of the correction on the ratio.

Image	Horizontal		Vertical	
	Ratio 1 (2/1)	Ratio 2 (2/3)	Ratio 1 (2/1)	Ratio 2 (2/3)
Fluorescence uncorrected	2.23	1.97	2.72	0.73
Red channel corrected fluorescence	2.37	2.14	2.17	0.82

2.3.2.3 Post processing

Figure 2.23 shows the intensity-pixel-graphs including the lower and upper threshold of the colormap. All three peaks are included as tumour and the background beneath the lower threshold. An intensity above 0.035 was marked as tumorous (red) and between 0.035 and 0.025 was marked as possibly tumorous (orange). All intensities below are marked as save, non-tumorous (green). Figure 2.24 shows that the same colormap can be applied to multiple exposure times and highlight the same areas. All five cups are marked as tumorous in the colormap. Although the differentiation is clearer for the higher exposure times. This correction and colormap, therefore, also shows the effect of tumour diameter and depth on the measured fluorescence intensity.

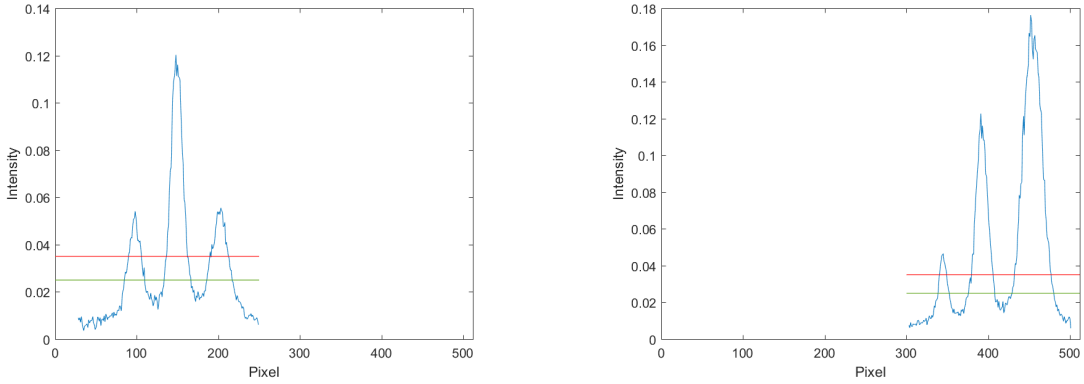

(a) Horizontal

(b) Vertical

Figure 2.23: Threshold for the colormap. The lower threshold is stated at 0.025 and the upper threshold at 0.035. This is based on gain of 10 and exposure of 800 ms

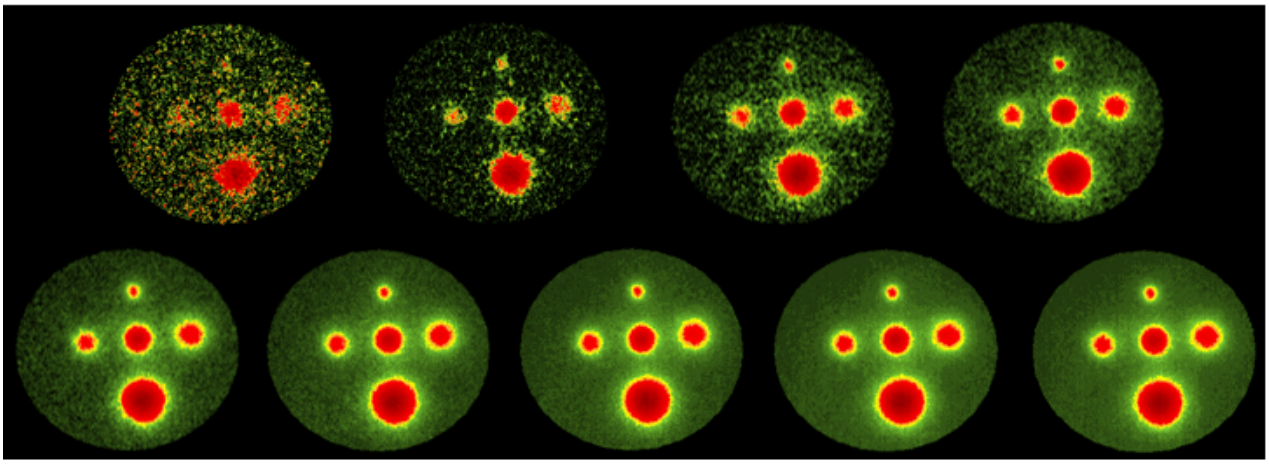

Figure 2.24: Colormap applied to all corrected images All images are scaled to an exposure time of one second and have a gain of 10. Top row are images with an exposure time from 50 - 200 ms and the bottom row from 400-6400 ms.

2.3.3 Analysis

Overall, the uncorrected fluorescence image shows a decrease in TBR with an increase in exposure time. The corrected fluorescence image shows an equal response. Remarkable is the high TBR for both images at an exposure time of 50 ms. The higher TBR at a low exposure time could be the result of the relatively dark background for the low exposure times. Resulting in a lower mean background value and therefore in a higher TBR. Opposite to the TBR, the SNR and CNR increase with an increase of exposure time.

Table 2.8: Overview of TBR, SNR and CNR values or all exposure times

	TBR		**SNR**		**CNR**	
Exposure time (ms)	Fluorescence uncorrected	Red channel corrected fluorescence	Fluorescence uncorrected	Red channel corrected fluorescence	Fluorescence uncorrected	Red channel corrected fluorescence
25	31.19	48.25	2.06	6.91	2.06	6.91
50	361.99	633.03	4.79	14.46	4.79	14.46
100	22.49	25.78	8.99	22.19	8.99	22.19
200	18.75	17.73	15.08	33.85	15.08	33.85
400	18.1	17.18	25.95	57.00	25.95	57.00
800	15.62	14.61	43.08	66.91	43.08	66.91
1600	14.93	13.96	66.11	92.22	66.11	92.22
3200	14.31	13.48	91.32	96.67	91.32	96.67
6400	14.13	13.29	114.18	99.51	114.18	99.51

2.4 Discussion

In this study, we investigated whether images could be normalized to generate absolute values to quantify fluorescence images. A 3D-printed phantom was created to validate a fluorescence normalization method. Our results showed that the correction method improved the fluorescence images for both the black box and intraoperative images. Furthermore, it is shown that for a phantom the excitation image and red channel image were equal when a correction factor is applied. Last, a generalised colormap was applied to visualize the difference between tumorous and non-tumorous tissue.

Our first finding showed that the intensity is linear with the exposure time for both the black box and the intraoperative camera, but the intraoperative camera saturated at higher gains. Therefore, the fluorescence images can be corrected for the exposure time by dividing the fluorescence images by the corresponding exposure time. Second, the difference between the red channel image and excitation image was analysed. An optimal threshold for the correction method was defined for both images and the effect of the correction was monitored. The correction showed that for the phantom both images could be used for the correction as they provided the same result. Finally, the result with the colormap showed that one colormap can be applied to multiple images and show the same result. Indicating that a single colormap could be possible to create a more universal map for differentiation between tumorous and non-tumorous tissue.

Previous studies [29, 32] showed the effect of a ratiometric correction on different concentrations of fluorescence. Both articles showed a positive effect by correcting the fluorescence image with the reflectance image. Furthermore, Upadhyay et al. showed the effect of the correction method when the camera had a variable distance and angle compared to the fluorescence. They showed as well that ratiometric correction with the white light image could correct for differences in illumination of the fluorescence. Our study differed from previous studies, in that it applied the correction on a thick (0.5 cm) solid phantom instead of liquid phantoms. It described the differences in correction between the excitation image and red channel images, as both are used by previous studies for the correction. Furthermore, it showed the effect of size and depth of the tumour spots on fluorescence intensity and that our method cannot correct for this effect. The applied ratiometric method has the disadvantage that it is performed on a pixel-by-pixel basis and therefore does not model the interaction of the pixel with neighbouring pixels. On the other hand, it is an easy to apply and a fast method.

Improvements for the study are mostly in the design of the 3D phantom and image acquisition. Although the 3D phantom provides a phantom that can be applied to repeat measurements, it has some drawbacks. The injection of the fluorescent tracer to the cups is more difficult due to the agar. The agar solidifies quickly when it gets in contact with the phantom, therefore, adjustments to the amount of solution is difficult. Furthermore, due to the shape of the cups, they induce surface tension and create bulging of the water. This results in an increase of the height of the cups. Last, it is not possible to create a completely homogeneous gelatine solution. This could be due to the India ink that does not fully dissolve in the gelatine solution. The acquisition of the images can also be improved. The polarization filter had to be manually adjusted, causing differences in intensity of the excitation image. Therefore, it is not possible to apply a correction factor automatically to the red channel image. The focus of the camera differs between the RGB image and fluorescence image. For an optimal correction, the image acquisition must be performed twice: once with the polarization and focus positioned for the RGB image and once for the fluorescence and excitation image. The correction method also has two main drawbacks. First the median filter is not linear, which could induce artefacts when processed. Second, resizing of the images could cause aliased noise, affecting the images.

This study showed that correction and application of an absolute colormap is possible for a homogeneous 3D phantom. Using the correction method, fluorescence imaging can become independent optical properties and illumination differences and show more genuinely fluorescence images. Therefore, these images show less influence of their surroundings and could be comparable between multiple

measurements. To transpose this method into a clinically viable method, the effect of heterogeneous tissue should be investigated on the correction method with both the excitation and red channel image and on the colormap. Furthermore, it could be to investigate if the measured fluorescence concentration could be linked to the measured fluorescence intensity. However, this could be limited because effect of size and depth of the fluorescence intensity and that it is not possible to correct for this yet.

2.5 Conclusion

Our correction method resulted in images which are corrected for various influences and show the fluorescence intensity according to an absolute colormap. This study validated the correction method, but further research with tissue should provide more information about the performance of this method on heterogeneous tissue.

3 | Performance of the ratiometric correction method on tissue

3.1 Introduction

Previously, the correction method was validated with a 3D phantom. In this part, the correction method will be applied to tissue and its performance will be analysed. Tissue is more heterogeneous, and the fluorescent spots are less well defined compared to the 3D phantom.

3.2 Method & Materials

Tissue samples were used from two completed studies: the TRACT study (NCT01972373) and the MARGIN study (NCT02583568). The TRACT study included patients with locally advanced rectal cancer who received neoadjuvant chemoradiotherapy and surgical resection. The MARGIN study included patients with breast cancer who were scheduled for breast cancer surgery (without neoadjuvant chemoradiotherapy). All patients received an intravenous bolus injection of 4.5 mg Bevacizumab-800CW, three days before surgery.

For both studies, the surgical specimen was sliced manually into 5 mm bread loaf slices and imaged with the black box. For the TRACT, these bread loaf slices were first fixed in formalin before imaging. Furthermore, some slices were imaged with an Odyssey scanner (confocal imaging). Last, the bread loaf slices were cut into smaller coupes and these were all imaged with the Odyssey scanner and HE staining was applied to the images to be able to perform tissue analysis. Per patient, one bread loaf slice was selected based on the presence of tumour tissue and clear odyssey scans and HE-coupes were present.

3.2.1 Correction method

The same correction method is applied as described in section 2.2.3 only this time to tissue slices instead of the 3D phantom.

3.3 Results

3.3.1 TRACT-study

3.3.1.1 Preprocessing

Effect threshold correction Figure 3.1 shows the visual effect of the threshold on the bread loaf slices. Correction with a percentage of 10 or 20% still shows a border-artefact due to under-illumination and subsequent division by low intensities. In the higher percentages, these border artefacts are reduced. Table 3.2 and 3.1 show the percentage of pixels that is adjusted and the corresponding threshold value for the red channel and excitation image, respectively. Where the percentages gradually increase in the red channel image, the increase is faster in the excitation image. As explained earlier, this could be related to the more homogeneous intensity of the excitation image. Furthermore, the percentages show more variation between patients for the excitation image compared to the red channel image. This could be the result of manually adjusting the polarization filter. A percentage of 30% was chosen for the red channel and 20% for the excitation channel, as we want to be close to 10% adjusted pixels for both images. This results in a mean adjusted percentage of 11.5% for the red channel and 15,3% for the excitation. So, the number of adjusted pixels is comparable.

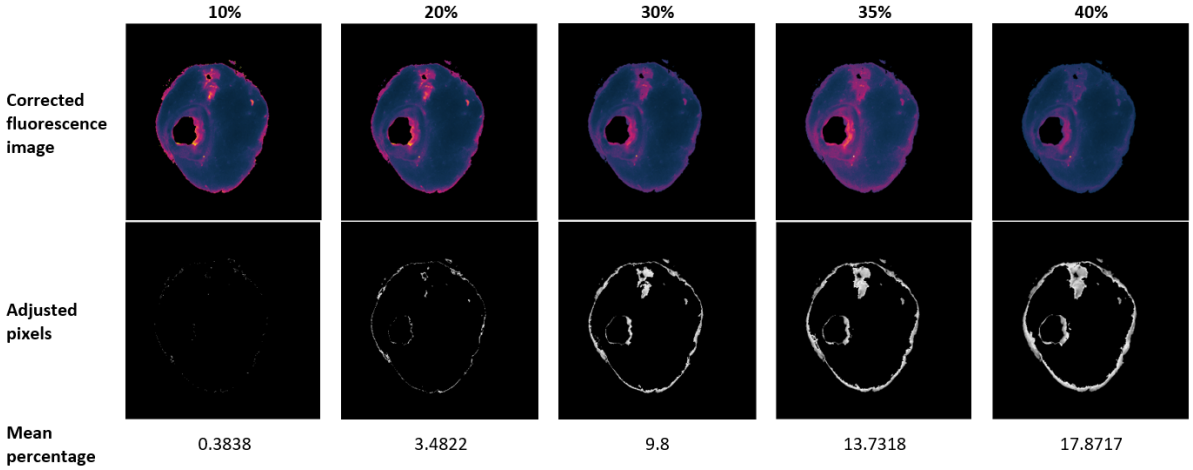

Figure 3.1: Effect of multiple thresholds on the corrected image.

Table 3.1: Excitation image corrected. The percentage of the image slice (zero pixels excluded) that is removed for multiple percentages

Patient	Percentage of maximum									
	10%		20%		30%		35%		40%	
	Percentage removed	Threshold value	Percentage removed	Threshold value	Percentage removed	Threshold value	Percentage removed	Threshold value	Percentage removed	Threshold value
1	1.8632	0.0017	4.7986	0.0034	10.1167	0.005	13.5293	0.0059	17.5429	0.0067
2	1.8825	0.0077	12.5462	0.0154	34.7693	0.0231	49.3213	0.0269	62.8588	0.0308
3	6.9189	0.0124	28.5337	0.0248	49.8311	0.0372	60.3368	0.0434	72.3367	0.0495
Mean	3.55	0.0073	15.29	0.015	31.57	0.022	41.06	0.025	50.91	0.029

Table 3.2: Red channel corrected. The percentage of the image slice (zero pixels excluded) that are removed for multiple percentages Three different patients are compared.

Patient	Percentage of maximum									
	10%		20%		30%		35%		40%	
	Percentage removed	Threshold value	Percentage removed	Threshold value	Percentage removed	Threshold value	Percentage removed	Threshold value	Percentage removed	Threshold value
1	0.4696	0.0500	3.3175	0.1	11.0540	0.15	15.4823	0.175	20.4659	0.2
2	0.3335	0.0510	3.1192	0.102	12.1130	0.153	17.9577	0.1785	24.8691	0.204
3	0.4824	0.0499	3.4822	0.0998	11.20	0.1497	15.7482	0.17465	21.0252	0.1996
Mean	0.4285	0.0503	3.3063	0.1006	11.45567	0.1509	16.39607	0.17605	21.92673	0.2012

Excitation vs. Red Channel Figure 3.2 shows a bread loaf slice of TRACT patient 3. For this patient the fluorescence, red channel and excitation image are shown, together with both corrected images. A red line is applied to the images to measure the intensity per pixel.

The correction factor between the excitation and red channel for TRACT 3 is measured to be (1/9.3). The intensity of both corrected fluorescence images seems to correspond quite well for its shape. However, the red channel (yellow) shows a higher intensity in the middle of the image. This could be the result of the dark spots visible in the RGB image (3.2B). These dark spots have a very low intensity, which could induce a higher intensity in the corrected images. The excitation image (red) shows border-artefacts on both side of the border.

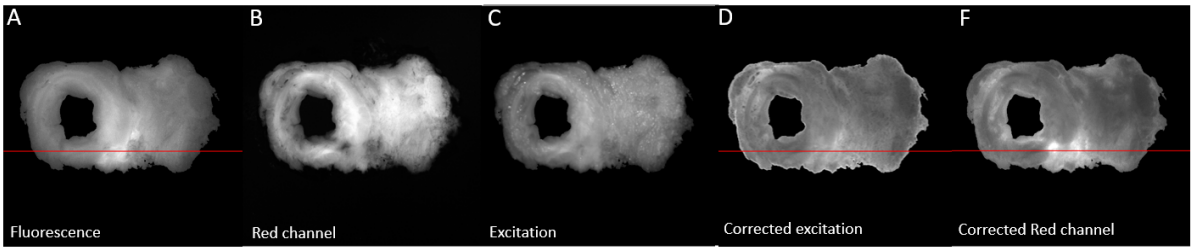

Figure 3.2: The effect of the correction with the red channel (30%) and excitation channel (20%).

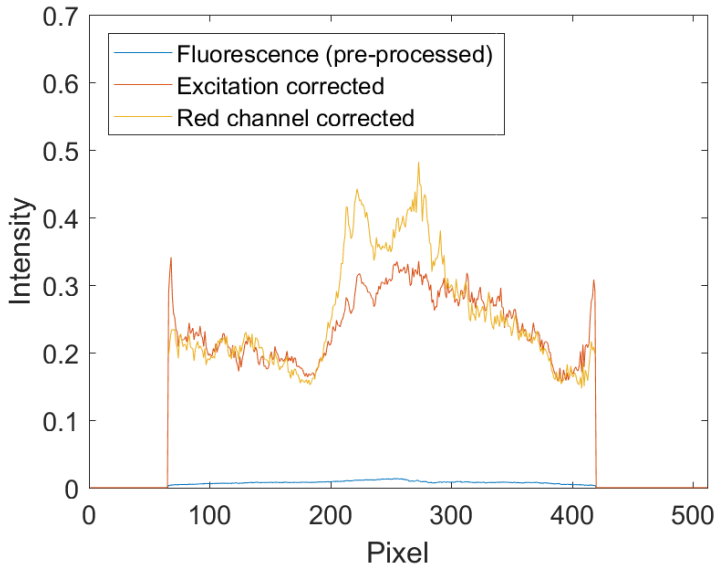

Figure 3.3: The effect of the correction with the red channel (30%) and excitation channel (20%).

3.3.1.2 Colormap

To determine the lower and upper threshold for the colormap, an intensity line is drawn in all three patients which includes fluorescent and non-fluorescent tissue (figure 3.4). The intensities corresponding to these lines are shown in figure 3.5. The background signals (non-fluorescent) are equal for TRACT 2 and TRACT 3. However, TRACT 1 shows a higher background signal compared to the other two. Therefore, one colormap for all three would not result in comparable images. The threshold values were therefore only based on TRACT 2 and TRACT 3. The lower threshold was set to 0.28 and the upper threshold to 0.31.

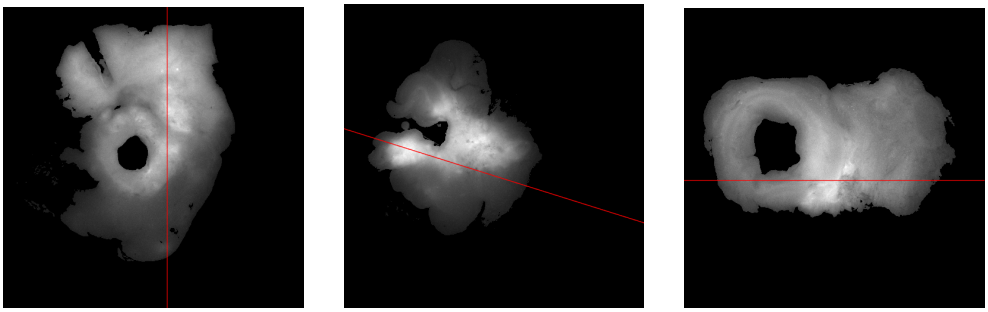

(a) TRACT 1 (b) TRACT 2 (c) TRACT 3

Figure 3.4: The position of the intensity lines for all three patients.

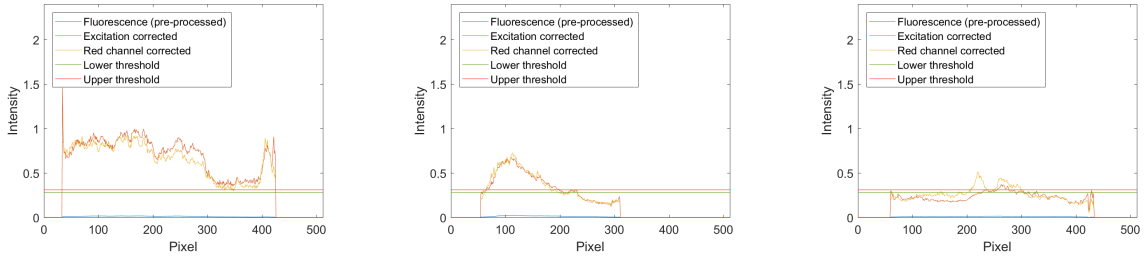

(a) TRACT 1: correction factor (1/26.4)

(b) TRACT 2: correction factor (1/9.8)

(c) TRACT 3: correction factor (1/9.3)

Figure 3.5: Intensity and corresponding thresholds

3.3.1.3 Correction method

Patient 1 Figure 3.6 shows that the corrected images are clearly different from the original fluorescence image according to the position of high intensities. This difference can already be seen in the differences in the red channel and excitation image. The excitation image is more equally illuminated compared to the red channel. The dark regions in the red channel cause the high intensities in the top left part of the bread loaf slice in the corrected images. Furthermore, both corrected images show a higher intensity in the bottom right part of the bread loaf slice which corresponds to a high vascularized lymph node. This was not visible in the uncorrected image, but is in the Odyssey scan (figure 3.7). For this patient it is difficult to determine which of the two corrections correspond better to the Odyssey scans and HE coupes. As mentioned before, the corrected intensities in this patient were higher compared to the other two patients. Therefore, the predefined colormap shows an almost red slice when applying the colormap.

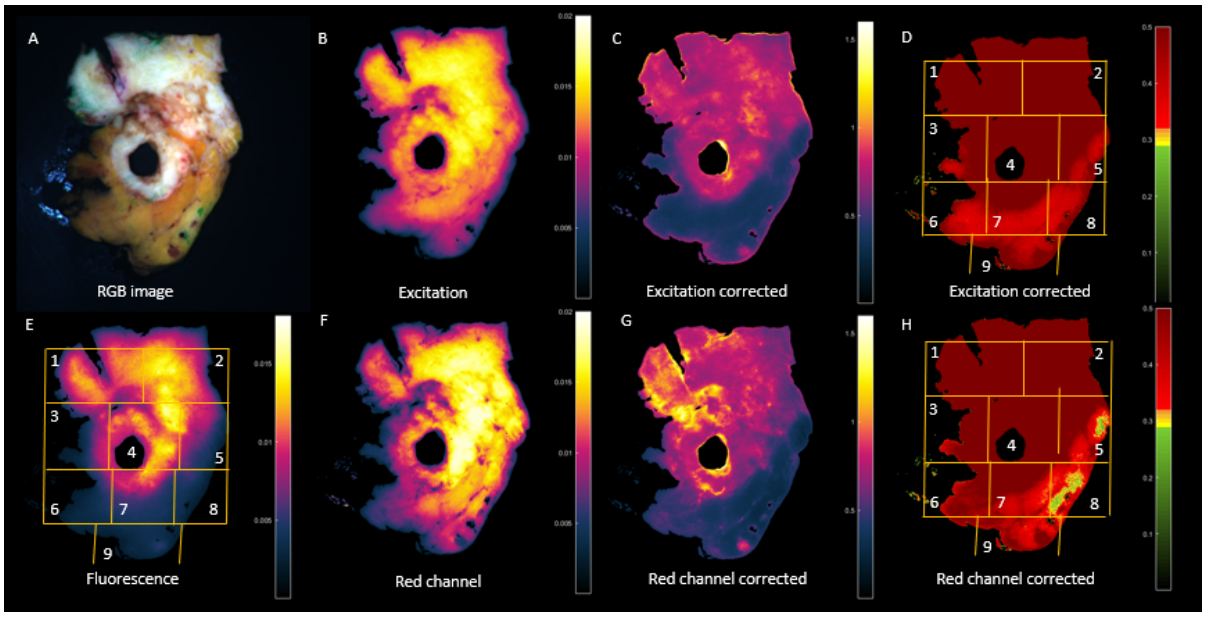

Figure 3.6: The effect of the correction with the red channel (30%) and excitation channel (20%).

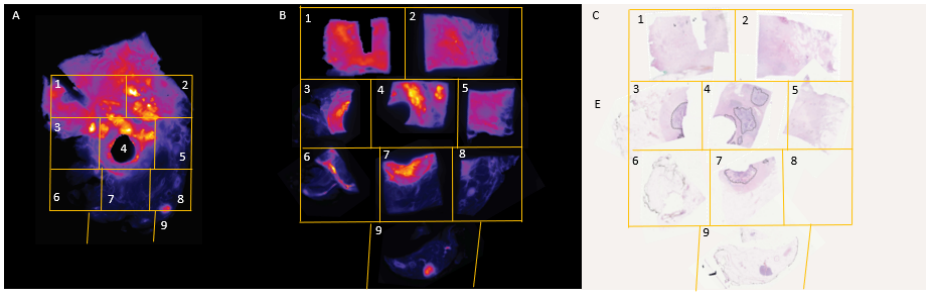

Figure 3.7: The validation images. A. Odyssey scan bread loaf slice B. Odyssey scan parts C. HE coupes

Patient 2 Figure 3.8 shows the effect of the correction for the second patient. Both corrections reduce the high intensity area a little and show the highest intensity in part 1, with the largest tumour area. The original fluorescence image (A) shows a larger area of high intensity compared to the Odyssey scan (F). However, in figure 3.9 the tumour can be seen to be spread through the whole bread loaf slice with a lot of small tumour spots and a bigger one on the left. The small tumour spots could cause additional scattering in the tissue, causing the blurred intensity region visualized in the corrected images. As the Odyssey scan is a confocal scan, scattering has less influence on the fluorescence intensity. The red channel corrected image seems to correspond more with the Odyssey scan compared to the excitation corrected image. When the excitation and red channel are covered with the colormap, not a big difference is visible between the two.

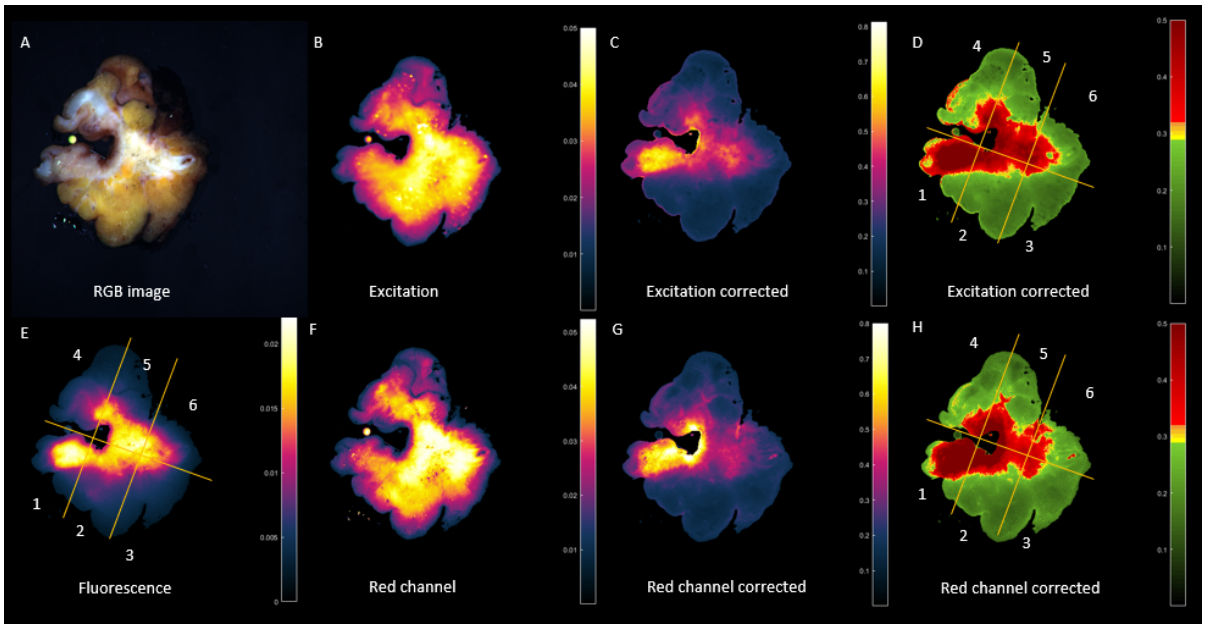

Figure 3.8: The effect of the correction with the red channel (30%) and excitation channel (20%).

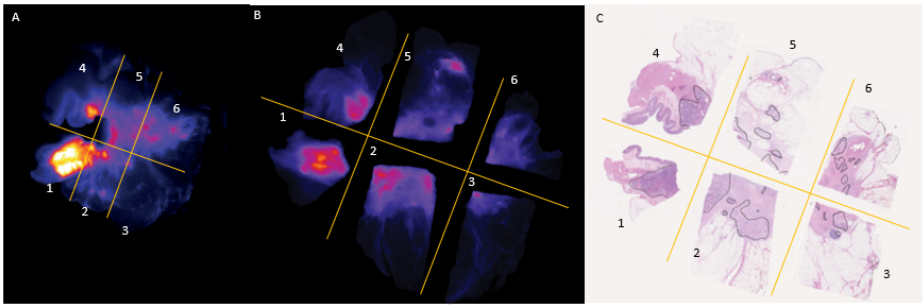

Figure 3.9: The validation images. A. Odyssey scan bread loaf slice B. Odyssey scan parts C. HE coupes.

Patient 3 Figure 3.10 shows the effect of the correction for both the red channel and excitation channel. The corrected images (C and F) show a difference in high intensities. A part of the high intensities in the red channel corrected image (D) is the result of the low intensity spot in red channel image (E), which is only visual in the red channel image and not in the excitation channel. On the other hand, the excitation corrected image has a high intensity spot at the top left, which could be the effect of low intensities as well. Furthermore, both corrections show an improvement of the original fluorescence image. Figure 3.11 shows an Odyssey scan, or confocal scan, of the same bread loaf slice, which seems to correspond well with especially the excitation image. Image B and C of figure 3.11 are thin slices, of a particular depth in the bread loaf slice. These show more accurately where the tumour is located and the HE stained images show where the tumour is exactly. The location of the tumour corresponds well to the visualized fluorescence in the Odyssey scans and corresponds well to the two corrected image, although the excitation corrected image seems to be a bit more accurate about the location.

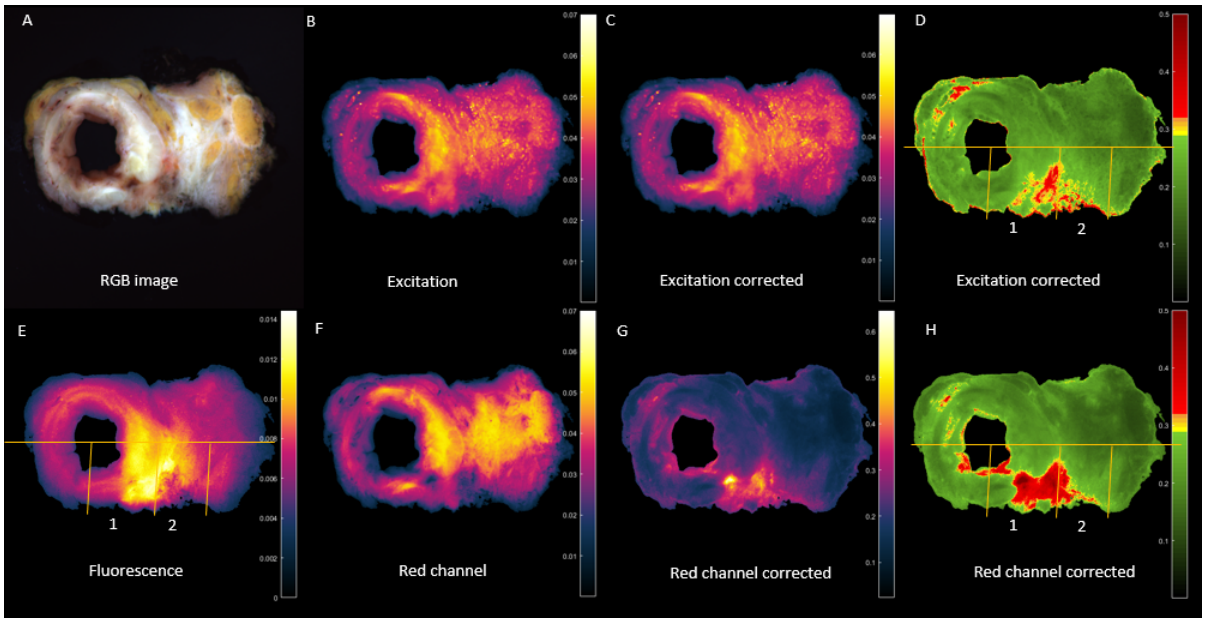

Figure 3.10: The effect of the correction with the red channel (30%) and excitation channel (20%).

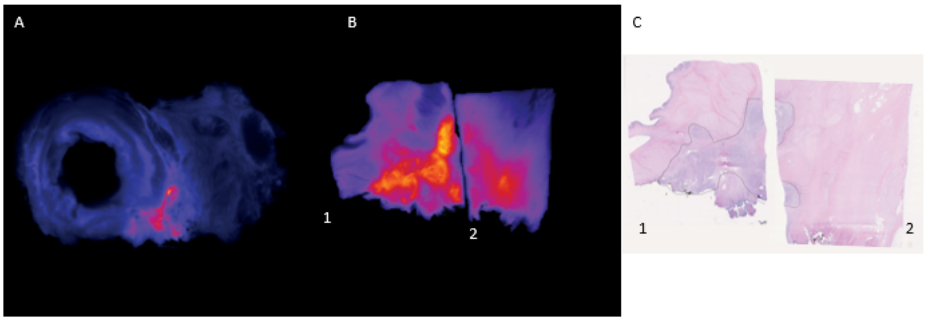

Figure 3.11: The validation images. A. Odyssey scan bread loaf slice B. Odyssey scan parts C. HE coupes

3.3.2 MARGIN-study

Similar to the TRACT study, we measured the effect of the threshold for both the excitation image and the red channel image. As we want to keep the total percentage adjusted pixels around the 10%, we chose a threshold of 20% for the excitation image and 30% for the red channel image.

Table 3.3: Effect of the threshold on the excitation image

Patient	10		20		30		40	
	Percentage Removed	Threshold value	Percentage Removed	Threshold value	Percentage Removed	Threshold value	Percentage Removed	Threshold value
101	2.68	0.0019	11.66	0.0039	23.1	0.0058	39.5	0.0077
102	2.50	0.0022	8.72	0.0043	18.0	0.0065	31,8	0.,0087
103	1.41	0.0019	8.17	0.0039	19.15	0.0058	36.58	0.0077
Mean	2.20	0.002	9.52	0.0040	20.07	0.0060	35.96	0.0080

Table 3.4: Effect of the threshold on the red channel

Patient	10		20		30		40	
	Percentage Removed	Threshold value	Percentage Removed	Threshold value	Percentage Removed	Threshold value	Percentage Removed	Threshold value
101	0.50	0.050	3.11	0.10	10.41	0.15	18.52	0.20
102	0.36	0.050	1.97	0.10	7.41	0.15	16.13	0.20
103	0.31	0.050	2.44	0.10	9.45	0.15	21.17	0.20
Mean	0.39	0.050	2.50	0.10	9.09	0.15	18.61	0.20

3.3.2.1 Colormap

Again, the lower and upper threshold were determined according to the intensity graphs of the three patients. An intensity line was drawn for all three patients and the intensities were measured for the uncorrected fluorescence and the corrected fluorescence with both the red channel and the excitation image. The corrected images show almost an equal signal. Only the red channel has a little higher peak in the middle of MARGIN 1. Also, a peak is visible at the border for both corrected images, which is probably a border artefact. Different from the TRACT patients, these patients all have equal background signal. Thus, tissue which does not include tumour or fluorescence, has the same intensity. According to these graphs, a difference in fluorescence intensity is visible between the tumours of the three patients. Therefore, the threshold was defined that at least these regions were shown as tumorous by the colormap. The lower threshold was set to 0.4 and the upper threshold to 0.44.

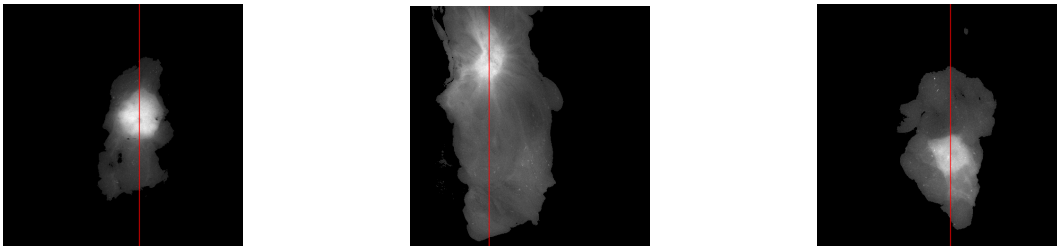

(a) MARGIN 101 (b) MARGIN 102 (c) MARGIN 103

Figure 3.12: Position of the intensity line

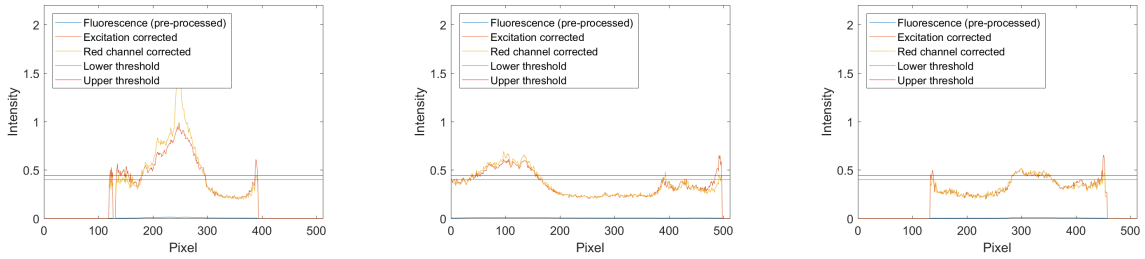

(a) MARGIN 101 (b) MARGIN 102 (c) MARGIN 103

Figure 3.13: Difference between the correction with the red channel and excitation channel.

3.3.2.2 Correction

Patient 1 Figure 3.14 shows the correction for the first patient. Both corrected images (C & F) show the tumour at the right location. However, both do not correspond fully to the Odyssey and HE coupes. The red channel seems to correspond a little better compared to the excitation channel. Furthermore, the excitation corrected image include some border artefacts due to division by low values.

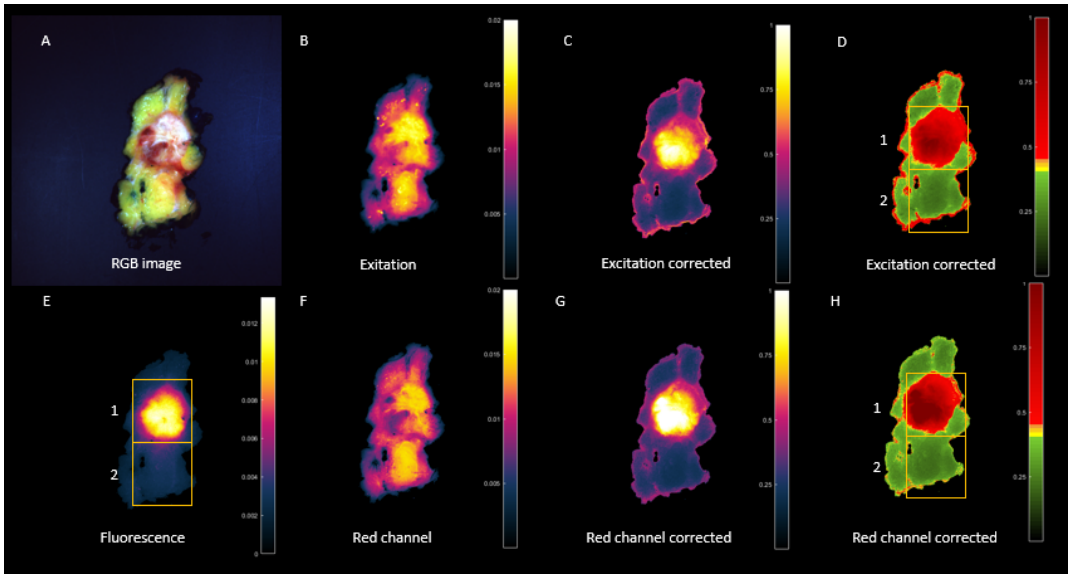

Figure 3.14: The effect of the correction with the red channel (30%) and excitation channel (20%).

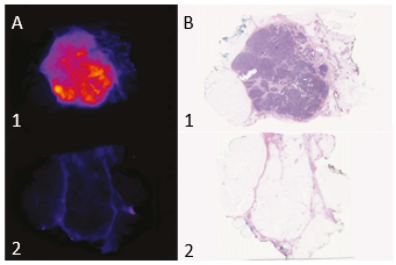

Figure 3.15: The effect of the correction with the red channel (30%) and excitation channel (20%).

Patient 2 Figure 3.16 shows the effect of the correction on the second patient. The excitation corrected images look similar, which is also visible on the images with colormap. Also in this patient, the excitation image has some border artefacts. The big area in the middle corresponds to tumour tissue, and the red area at the left side corresponds to skin, which shows high fluorescence as well.

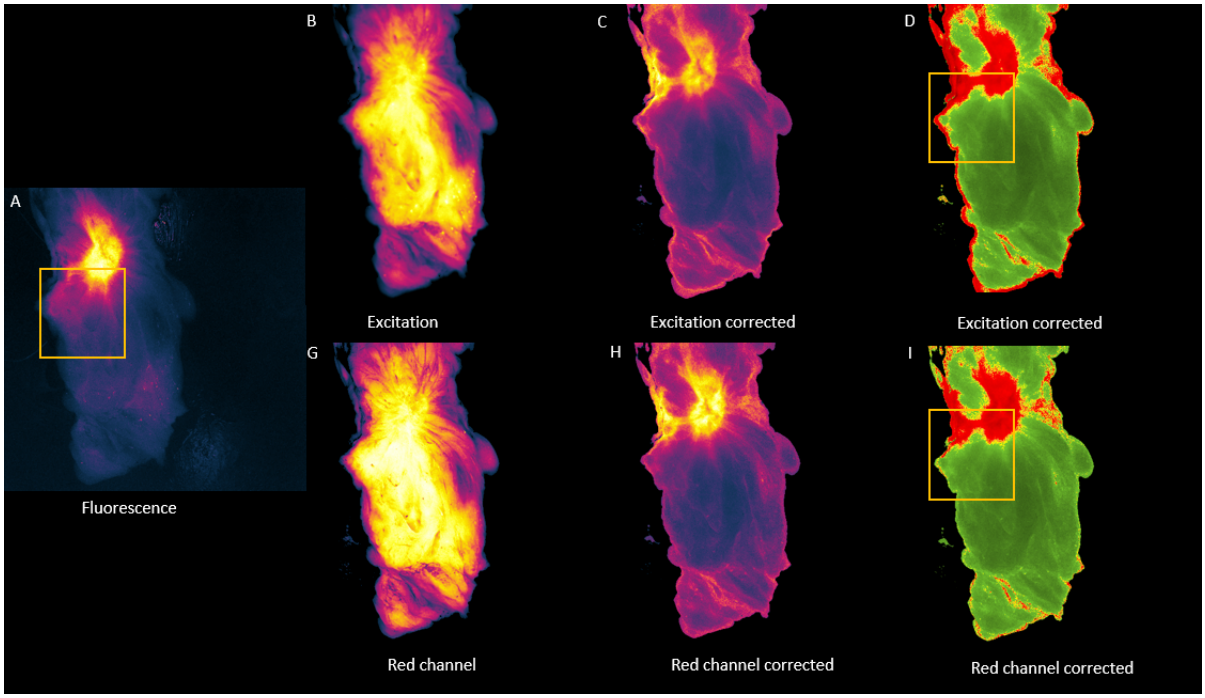

Figure 3.16: The effect of the correction with the red channel (30%) and excitation channel (20%).

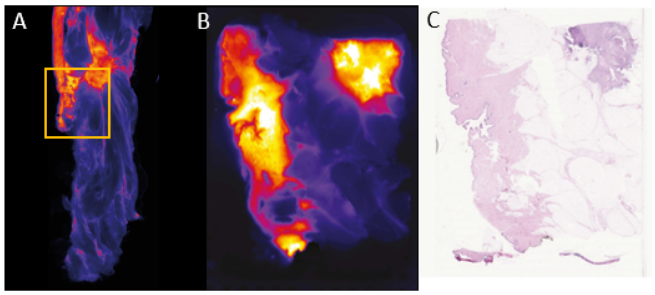

Figure 3.17: The effect of the correction with the red channel (30%) and excitation channel (20%).

Patient 3 Figure 3.18 shows that both corrected images show a higher intensity in the middle of the bread loaf slice and border artefacts. Only small differences can be seen between the corrected images.

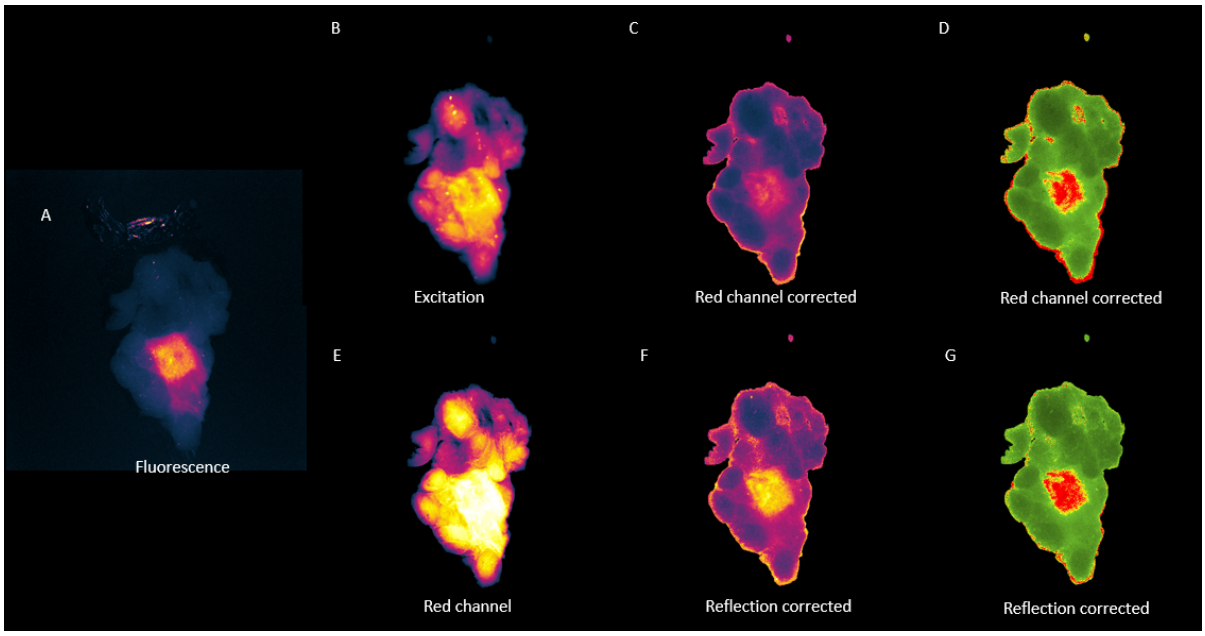

Figure 3.18: The effect of the correction with the red channel (30%) and excitation channel (20%).

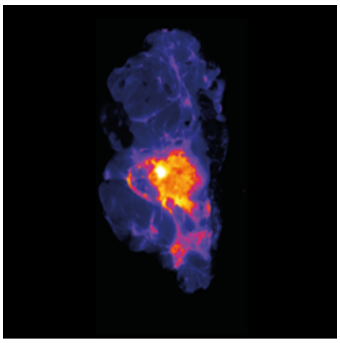

Figure 3.19: The effect of the correction with the red channel (30%) and excitation channel (20%).

3.4 Discussion

In this study, we investigated the performance of the previously developed correction method on two types of tissue. Our results showed an improvement of the fluorescence images for both tissue types, but the extent of the improvement differed between the two tissue types.

The results showed that more variation is visible in the intensity-pixel graphs between the excitation and red channel corrected fluorescence images, because of intensity differences in the excitation and red channel images. These variations could be the result of the more heterogeneous tissue compared to the more homogeneous 3D phantom or because the red channel is more susceptible for low intensity areas within the RGB image or both. These low intensity areas cause high intensity areas in the corrected fluorescence images, although these values are not induced by optical properties or illumination differences. The effect of the correction was better visible in the TRACT study because of higher variance in tumour areas, compared to the MARGIN which includes more localized tumours. Although our images do not show a clear preference for excitation or red channel correction, excitation is preferred, for further investigation. The excitation image covers all wavelengths and no filter is applied. Therefore, the information within the excitation image consists of the full range of wavelengths and gives a more realistic overview. The RGB image on the other hand, only ranges from 400-700 nm and includes a filter.

Multiple border artefacts were visible in both corrected images, especially in the excitation corrected images of the MARGIN study. Descending boundaries of the bread loaf slices might have caused a decrease in measured intensity and therefore in lower values. Furthermore, some of the slices were inked for pathology, increasing the absorption of the light. The threshold did not remove all low values, resulting in the high intensity border artefacts. These two effects could indicate that a higher threshold for correction might be justified for these images. Additionally, all images were acquired before the start of this study, resulting in images that were not always acquired optimally. Both the polarization filter and focus of the camera were not always optimally positioned for acquiring both the fluorescence and RGB image. The position of the polarization filter is dependent on the wavelength and therefore differs between the fluorescence and RGB image. A general drawback of this correction method is that it cannot correct for scattering effects and for the dependence of light intensity to depth. Where scattering effects can alter the measured fluorescence intensity and delineation of the tumour, the dependence of light intensity to depth limits the differentiation between a high concentration at a great depth or a superficial low concentration.

This correction method improves the visualization of fluorescence in tissue and comparison between patients. Intra-operatively this could give a better visualization of resection margins as areas with low illumination or higher absorption are corrected for by this method. Furthermore, this method can reduce the effect of distance and angle of the camera to the tissue improving comparison between multiple images made during surgery. This effect could also improve endoscopic fluorescence imaging, as the effect of distance and angle is even more dominant at this procedure. The limitation of this method on the scattering and depth correction can result in areas that show a higher fluorescence intensity or incorrect delineation of the tumour due to scattering effects. The dependence on depth could make it difficult when a high intensity tumour is close to the resection margin and therefore is showing fluorescence on the outside. However, this could be verified by imaging the wound bed as well. Endoscopy procedures for therapy assessment could be affected more by the depth dependence of fluorescence intensity, as no difference can be made between high fluorescence in deep tissue or superficial low fluorescence determination of the therapy effect is more difficult.

Improvements for following studies would be the acquisition of the images and determination of the optimal correction and colormap threshold. The suboptimal acquisition of the tissue images induces inaccuracies and uncertainties in the results. These inaccuracies could be reduced, ex vivo, by obtaining the images twice with different settings. Once with optimal settings for the fluorescence and excitation image to perform the correction and once for an optimal RGB image for validation. Automatic or pre-

defined settings for the polarization filter and focus would simplify image acquisition. Furthermore, with optimal acquired images, both threshold could be defined more accurate. Last, this study only investigates the threshold for patients injected with 4.5 mg bevacizumab-800CW the effect of other tracers and dosages should be investigated as well.

To incorporate this ratiometric correction clinically, it is important that a simultaneously acquired excitation image is available instead of only an RGB image. For automatic correction, fixed or predefined settings in the polarization filter are necessary, to reduce variations and therefore inaccuracies between patients. Extended research should be necessary to estimate the optimal thresholds for the correction and colormap and define the corresponding sensitivity and specificity. These thresholds probably must be defined depending on tumour type and tracer concentration. Last, real time correction of the images would be optimal for implementation. Further research should examine if this is possible with the current fluorescence device used.

3.5 Conclusion

In summary, our study shows that our correction method improves the visualization of fluorescence images of tissue, although the performance of the applied colormap differs between the two cancer types. Further investigation should improve image acquisition and the correction method. Clinically, the imaging devices should be adjusted to acquire excitation image simultaneously and if real time imaging is possible.

4 | Space-variant deconvolution

4.1 Introduction

The acquired fluorescence images show a blurred fluorescence signal due to optical properties affecting the propagation of light in the tissue. Each tissue has a specific absorption and scattering coefficient, influencing the NIR light applied by the imaging systems. In the NIR light, scattering is dominant over absorption, causing degradation of the measured images and loss of information about tracer concentration and tumour delineation. Previously, a ratiometric correction method as applied to reduce the influence of optical properties and imaging system parameters. However, this method is a pixel-by-pixel correction method which does not involve the contribution of neighbouring pixels. As scattering influences its surrounding by loss of directionality, a more advanced method is necessary to account for this effect.

The scattering effect can be considered as blurring of the image. Improvement of the fluorescent image would then be achieved by deblurring of the images. However, in the images the amount of blurring is often unknown and varies per tissue. A possible way of improving the blurred image is with spatially-variant deconvolution, as proposed by Glatz [35]. Here, a specific scattering coefficient is determined per pixel to correct for spatially varying scattering within the tissue. However, deconvolution is an ill-posed problem and can only recover information that is already present in the blurred image. Therefore, the deconvolved image approximates the ideal image. However, it could help improving the blurred image and creating a more realistic fluorescence image.

In this study we want to apply a spatially-variant deconvolution inspired on the method used by Glatz. The goal is to calculate the scattering coefficient for multiple tissues and apply a space-variant Richardson-Lucy deconvolution to reduce the blurring and enhance the fluorescence images.

4.2 Materials & methods

4.2.1 Materials

4.2.1.1 Black box

The black box (Surgvision, The Netherlands) consists of four LED lights, a lens, a filter wheel and a digital CMOS camera (figure 4.1). Two of the LED's were used for white-light (400-700 nm) illumination and two for NIR illumination (>700 nm). The two white LED's (gray in figure 4.1) and the two NIR lights (red in figure 2.3) were positioned on diagonally opposite sides above the sample, forming a square with the white-light LED's. The white light LED's were used for acquiring an RGB image (colour registration) and the NIR LED's for acquiring the fluorescence and excitation image. In front of the lens, a polarisation filter is located that can be manually adjusted. This polarisation filter decreases the specular reflections from the surface and was applied for all images. On top of the lens a filter wheel is located. For each image another filter was used. For the RGB image, three filters were applied independently (see table 2.2). So, the red, blue and green images were taken after each other, ultimately creating one RGB image with a fixed exposure time of 40 ms. For the fluorescence image, two filters, a bandpass and longpass filter, were used simultaneously. The NIR LED applied a narrow spectrum (<10nm), peaked at 760 nm. The exposure time of the fluorescence image can be manually adjusted. For the excitation image, no filter is applied, and the image was made with a fixed exposure time of 20 ms. All images are captured with a digital CMOS camera. Finally, the images are viewed and stored on a computer.

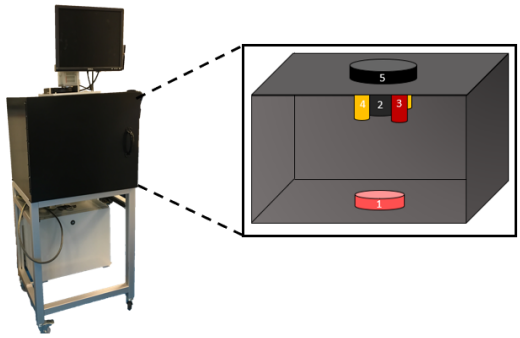

Figure 4.1: Overview of the black box. 1. Bread loaf slice. 2. Camera lens + polarisation filter. 3. NIR LED's 4. RGB LED's 5. Filter wheel.

4.2.1.2 Phantom

The modified Shepp-Logan model, which is a model of a human head, was used as a mathematical phantom for the deconvolution method. The size was defined as 256x256 pixels.

4.2.1.3 Tissue

Tissue samples were gathered from the TRACT study (NCT01972373), which included patients with locally advanced rectal cancer that received neoadjuvant chemoradiotherapy and surgical resection. Afterwards, the surgical specimen is sliced into 5 mm bread loaf slices and imaged with a black box. All patients received an intravenous bolus injection of 4.5 mg Bevacizumab-800CW, three days before surgery. The bread loaf slices were formalin fixed for two days.

Analysis is previously done with the black box, Odyssey scanner (confocal imaging) and HE staining. This previously acquired data is used in this study.

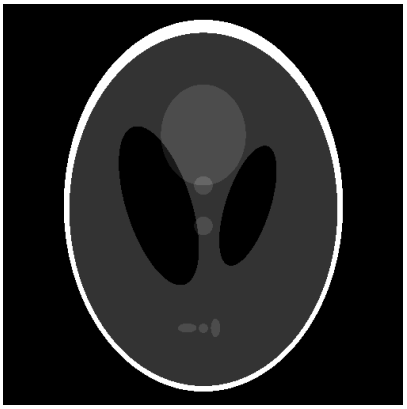

Figure 4.2: Shepp-Logan model

4.2.2 Theory

4.2.2.1 Convolution

A convolution is a mathematical operation which takes an original signal and a point spread function (PSF) as input and produces a third, blurred signal as output. The convolution of two signals $f(t)$ and $g(t)$ is defined as an integral transform:

$$y(t) = (f * g)(t) = \int_{-\infty}^{+\infty} f(t-\tau)g(\tau)d\tau + n \tag{4.1}$$

where $y(t)$ is the blurred fluorescence image, $f(t)$ is the original, intrinsic fluorescence image, $g(t)$ is the PSF modelling the blurring and n is the noise added to the blurred image. The minus sign accounts for the flipping of the kernel 180°and τ is an integration variable. In our method the noise will be neglected for further calculations.

Equation 4.1 applies only to continuous signals, however, the acquired measurements are blurred fluorescence images. Digital images are represented as a discrete 2D array $I[x, y]$. Therefore, the convolution must switch from a continuous to a discrete formula and extension is needed to go from 1D to 2D. Therefore, the integral is substituted for a summation.

$$(I * K)[x][y] = \sum_u \sum_v I[x-u][y-v]K[u][v] \tag{4.2}$$

where $I[x, y]$ is the original image and $K[u, v]$ is the point spread function or kernel. This equation is spatially invariant as the PSF does not depend on the position in the output image. The convolution of an image with a point spread function or kernel is visualized in figure 4.3.

Point spread function (PSF) In the spatial domain, the PSF describes the extent of optical blurring of a point or pixel because of multiple influences like image acquisition and optical properties. The PSF is often represented as a rotationally symmetric 2D Gaussian function (equation 4.3), which is a low-pass filter, attenuating high frequency components of an image.

$$G(x, y) = \frac{1}{2\pi\sigma^2} e^{-\frac{x^2+y^2}{2\sigma^2}} \tag{4.3}$$

where x and y determine the size of the point spread function and σ is equal to the standard deviation of the Gaussian function and describes the width of the function. The greater the σ, the wider the Gaussian

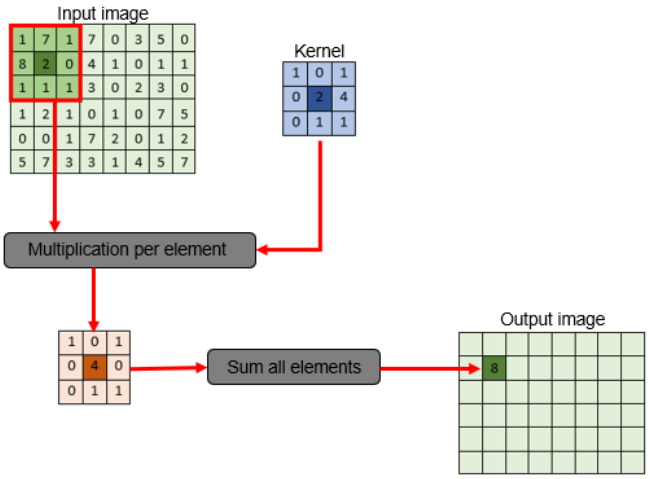

Figure 4.3: Convolution using a 3x3 kernel. All elements in a 3x3 window in the input image are pixel-by-pixel multiplied with the kernel elements. The elements of the resulting 3x3 matrix are summed resulting in one final value.

filter and the more smoothing of the image occurs.

An imaging system with the same PSF at all locations in the field of view is called spatially invariant, thus the blur is independent of its position. While a system that is dependent on its position is called spatially variant (figure 4.4). Here, each pixel has a specific blur which can differ from other pixels.

(a) Spatially invariant PSF (b) Spatially variant PSF

Figure 4.4: Point spread function (PSF) [34]

4.2.2.2 Deconvolution

Deconvolution is the reverse operation of the convolution; where the original image is obtained from the PSF and the blurred image. However, deconvolution is an ill-posed problem, due to amplification of the noise and suboptimal deconvolution. For ill-posed problems the output does not depend continuously on the input. This means in particular that it is often not possible to recover a unique solution and thus not the exact original image. The accuracy and quality of the PSF are essential to ensure correct performance of the (de)convolution algorithm. Therefore, the accuracy of the deconvolved image is dependent on the accuracy of the PSF used for the deconvolution.

In this study, we apply spatially variant deconvolution, where the PSF changes with the images location. So, the PSF will change with the pixel coordinates [u][v]. For a spatially variant deconvolution, the convolution can be expressed as:

$$(I * K)[x][y] = \sum_{u} \sum_{v} I[x-u][y-v]K[u][v](x,y) \tag{4.4}$$

Frequency domain Convolution in the spatial domain is time consuming, to accelerate the calculation, a Fourier transform is applied to the signals. The Fourier transform encodes the amplitude and phase of each frequency component. Transforming the PSF to the frequency domain results in the optical transfer function (OTF). The advantage of the frequency domain is that the signals can be multiplied instead of applying a convolution.

As mentioned before, the PSF and thus the OTF, is a low-pass filter. Thus, convolution of the object by a PSF attenuates high-frequency (small features and edges) components more than low frequency components (large features and smooth areas). Therefore, the deconvolution boosts high spatial frequency components more than low spatial frequency components. However, noise is present in all frequencies, but especially in high-frequency components. Thus, by increasing the high frequency components, noise is also increased during deconvolution.

As the convolution in spatial domain is equivalent to multiplication in the frequency domain, deconvolution should be equally to the division of the blurred image by the PSF in the frequency domain (Fourier transform). Although this is mathematically true for the deconvolution, this operation is not feasible due to the strong amplification of noise. Therefore, other deconvolution methods are needed to obtain the original image.

Richardson-Lucy deconvolution The Richardson-Lucy deconvolution calculates the maximum-likelihood solution to a deconvolution problem by performing a series of iterative convolutions. It assumes that the noise follows a Poison distribution. The Richardson-Lucy algorithm has two important properties: non-negativity and energy preservation. However, the method multiplies both the magnitude of the signal and the ringing artefacts around the edges at each iteration. Therefore, the more iterations, the stronger the ringing artefact is in the restored image [36].

$$I_{n+1} = I_n \left(\frac{C}{I_n * K} \right) * \bar{K} \tag{4.5}$$

Where I_n is the reconstructed or deblurred image at iteration step n, C is the observed blurred image, K is the PSF and $\bar{K}$ is the kernel flipped along both coordinate axes.

Lucy-Richardson is based on forward convolution. The method works by iteratively comparing an estimate of the intrinsic image with its blurred image. First, Richardson-Lucy iteratively compares an estimate of the original image with the blurred image. The initial estimate of the original image is convolved with the PSF to make an estimate of the true image. At any iterative cycle, n, the running estimate of the source is convolved with the PSF to make an estimate of the true image. In our study, the blurred image will be applied as the first estimate.

$$E_n = I_n * K \tag{4.6}$$

A correction image is then estimated by convolving a ratio of the estimated image by the transposed kernel.

$$R_n = \left(\frac{C}{E_n} \right) * \bar{K} \tag{4.7}$$

This is used to update the source estimate by multiplication with the correction image.

$$I_{n+1} = I_n R_n \tag{4.8}$$

Each iteration thus requires one convolution of the PSF with the source, and one convolution of the image to estimated-image ratio with the PSF transpose [37].

Table 4.1: The scattering coefficient and sigma for multiple tissues at 800 nm [38, 39].

	μ_s'(cm)	μ_s' (pixels)	**Sigma**
Fat	13,8	3	5
Blood	16,5	4	6
Fibrosis	12,6	3	5
Mucosa	13	3	5

Equation 4.5 was extended to a spatially variant deconvolution by replacing the two spatially invariant convolution operations a spatially variant convolution resulting in equation:

$$I_{n+1} = I_n \frac{C}{I_n * K[u][v](x,y)} * \bar{K}[u][v](x,y) \tag{4.9}$$

Iterations Iterations are the amount of repetitions of the process. A trade-off must be made between reaching the desired solution (high number of iterations) at convergence and reduction of noise amplification (low number of iterations).

4.2.3 Method

4.2.3.1 Segmentation

Phantom The phantom is blurred in two ways: one spatially invariant and one spatially variant. The spatially invariant is blurred with a sigma of both 5 and 6. The spatially variant image is divided in two intensities. Everything below 0.2 has a sigma of 5 and all pixels above have a sigma of 6.

Tissue The image is converted from a RGB image to a HSV image. HSV stands for Hue, Saturation and Value and is more closely aligned with the way human vision perceives colour. Next, colour thresholding is applied to obtain the threshold values for multiple tissues: fat, blood, fibrosis and mucosa. For each tissue the scattering coefficient (μ_s') is defined at 800 nm (table 4.1). However, as not all scattering coefficients are known at the right wavelengths, a conversion method is used [38]:

$$\mu_s'(\lambda) = a \left(\frac{\lambda}{500nm} \right)^{-b} \tag{4.10}$$

where b is called the 'scattering power'. This term characterizes the wavelength dependence of μ_s'. The factor a is the value $\mu_s'(\lambda = 500nm)$, which scales the wavelength-dependent term. Both factor a and b are the mean values acquired from multiple articles.

The scattering coefficient is converted from cm^{-1} to pixels to be able to apply to the images. Assumed is that the average scatter will be at the middle of the bread loaf slice, thus at 2.5 mm. Therefore, the reduced scattering coefficient is multiplied by the depth, resulting in the coefficient in pixels (0.25). Finally, the scattering coefficient in pixels is summed with the maximal resolution of the system in pixels. All values are rounded up. The resolution of the black box is estimated at 124 μm in 512 pixels, resulting a value of 4. However, we resize the images to 256 pixels, due to computational reasons. Therefore, the resolution is changed to a value of 2.

Kernel size The kernel size is generated by equation 4.11. Depending on the sigma assigned to the pixel, the PSF is calculated. The PSF is a 2D gaussian kernel with a standard deviation of sigma. All

PSF are saved in a PSF matrix, in which each pixel consists of a particular PSF.

$$Size = 2 * ceil(2 * \sigma) + 1 \tag{4.11}$$

The kernels at all locations (x,y) are normalized so that:

$$\sum_{u} \sum_{v} K[u][v](x, y) = 1 \tag{4.12}$$

4.2.3.2 Spatially variant deconvolution

The space-variant deconvolution is based on the deconvlucy algorithm in MATLAB. This algorithm is modified to be able to apply spatially variant deconvolution in Fourier space and based on the method according to Biggs et al. [40]. First, the PSF matrix is converted to an OTF matrix by applying a Fourier transform. The first estimate of the unblurred image I_n is stated as the blurred image. Pixel-by-pixel the image is convolved with the corresponding OTF and the resulting image E_n is added to a big matrix were all resulting images are added. Therefore, the effect of the neighbouring pixels is summed resulting in one big estimate of the true image. Next, the same step is made with the convolution of the ratio with the flipped kernel resulting in an updated estimate of the true image.

4.3 Results

4.3.1 Segmentation

4.3.1.1 Phantom

The phantom is divided into two sections based on the intensity of the pixels by a threshold of 0.2.

(a) Original image

(b) High intensity part segmentation

(c) Low intensity part segmentation

Figure 4.5: Segmentation of the phantom image

4.3.1.2 Tissue

The tissue slice is divided with a threshold into three main sections based on the colours of in the HSV image. Each section has its own scattering coefficient and based on that, the corresponding sigma is calculated for the deconvolution.

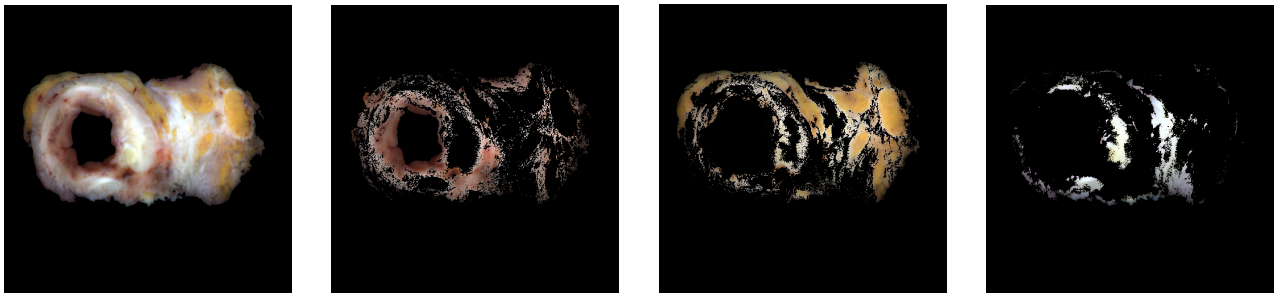

(a) Original image (b) Red pixels, close to blood or mucosa (c) Yellow pixels, close to fat (d) White pixels, close to skin

Figure 4.6: Segmentation of the tissue slice

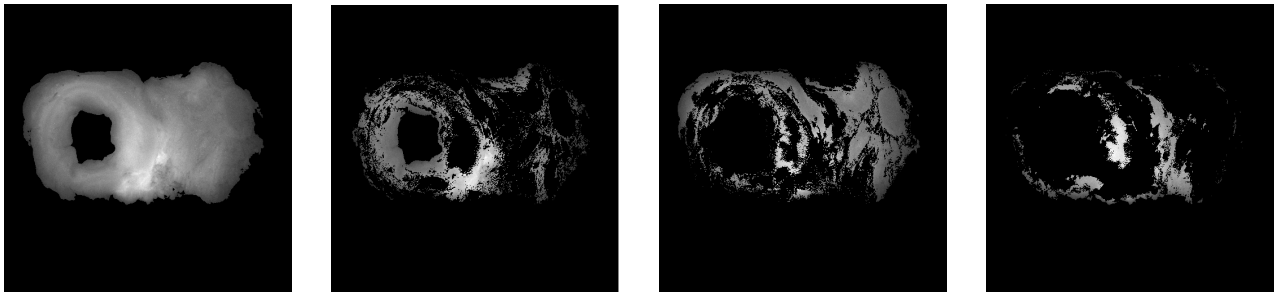

(a) Original image (b) Red pixels, close to blood or mucosa (c) Yellow pixels, close to fat (d) White pixels, close to skin

Figure 4.7: Segmentation of the phantom image shown with the excitation image.

4.3.2 Phantom: Spatially invariant deconvolution

4.3.2.1 Variables

Sigma The sigma determines the amount of blurring. The higher the sigma, the higher the blurring and often the more difficult it is to acquire a good result after deconvolution.

(a) Sigma = 2 (b) Sigma = 4 (c) Sigma = 6 (d) Sigma = 8

Figure 4.8: The effect of sigma on the shape of the kernel

Kernel size The size of the kernel influences the deconvolution result. As we have multiple sigma's in the space-variant deconvolution, but only one kernel size, this could influence the resulting image. A small kernel compared to a right-sized kernel for the sigma can cause a less sharp image after the same amount of iterations. Furthermore, a kernel that is too big, can cause more ringing artefacts. Especially

when a higher sigma is applied, as it is more difficult to obtain the original image as the image is more blurred. Last, each iteration will amplify the effect of the kernel.

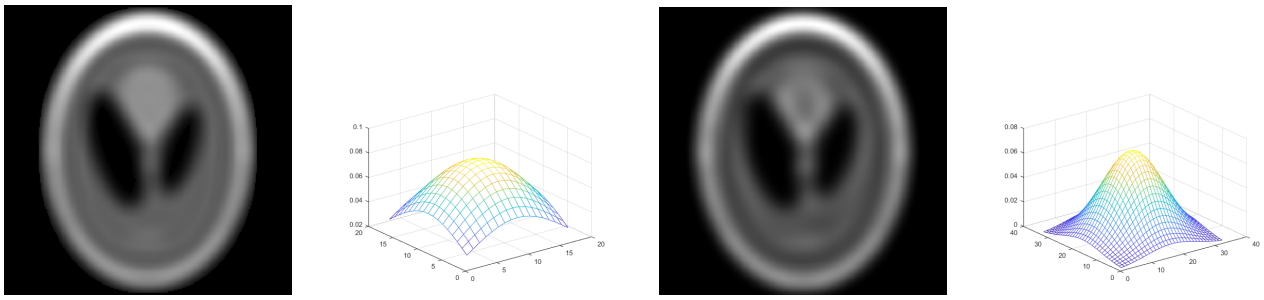

(a) Sigma = 8, kernel size = 17

(b) Sigma = 8, kernel size = 17

(c) Sigma = 8, kernel size = 33

(d) Sigma = 8, kernel size = 33

Figure 4.9: The effect of the kernelsize

Iterations An increase in iterations creates an increase in sharpness, but also an increase in ringing artefacts. Furthermore, the intensity of the inner part of the phantom is lowered, reducing the contrast in the image.

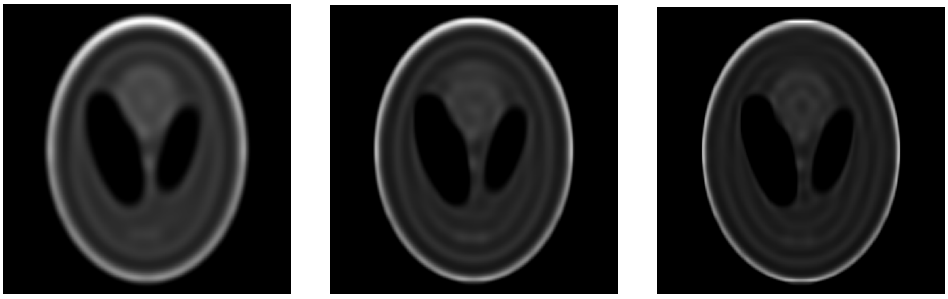

(a) 10 iterations

(b) 25 iterations

(c) 50 iterations

Figure 4.10: The effect of the amount of iterations. All images were blurred with a sigma of 6 and a kernel of 25 pixels

4.3.2.2 Comparison methods

Our modified code was compared to the unmodified Richardson-Lucy algorithm to validate if our method worked sufficient. Two equal sigmas were used in our modified spatially variant deconvolution, so it acted like a space invariant deconvolution. The results of our modified code were correlated to the unmodified Richardson-Lucy algorithm. Both images show equal results after application of the deconvolution.

(a) Uncorrected blurred image

(b) Unmodified Richardson-Lucy algorithm

(c) Our modified Richardson-Lucy algorithm

Figure 4.11: Both images were made with a sigma of 8, a kernel of 33 pixels and after 10 iterations.

4.3.3 Phantom: Spatially variant deconvolution

Figure 4.12 shows the effect of space-variant deconvolution for two different kernels. Both images show an increase in sharpness but also an increase in size of the two black areas within the phantom. The larger kernel size also effects these black areas. The larger kernel size results in a larger area.

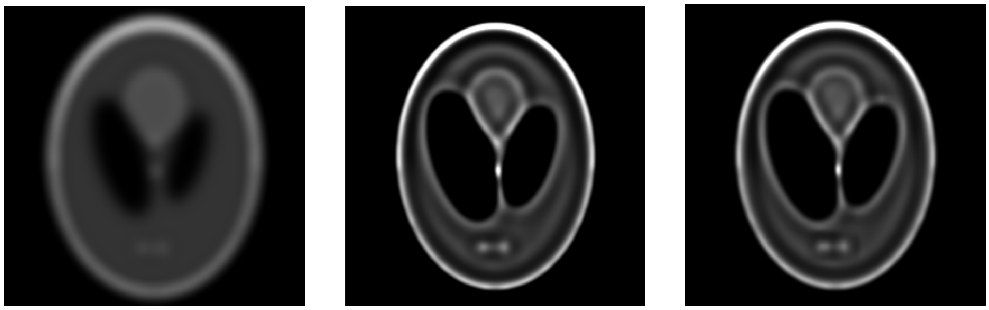

(a) The blurred image

(b) Deconvolution with a kernel size of 33

(c) Deconvolution with a kernel size of 35

Figure 4.12: Spatially variant deconvolution of the phantom with a sigma of 4 and 5, 10 iterations and two different kernels (33 and 35).

4.3.4 Tissue: spatially variant deconvolution

The spatially-variant deconvolution of tissue shows the tissue with only small high intensity spots where there should be tumour. Although only small spots are visible, they are at the right position. Furthermore, multiple border artefacts are visible and the black area within the tissue is larger as it was also in the phantom images.

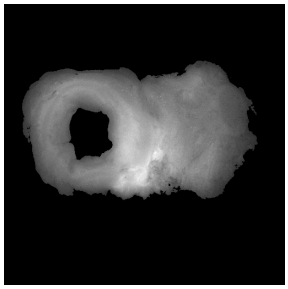

(a) Original masked fluorescence image

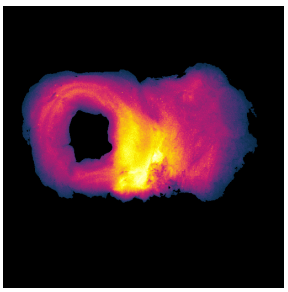

(b) Original masked fluorescence image with fire colormap

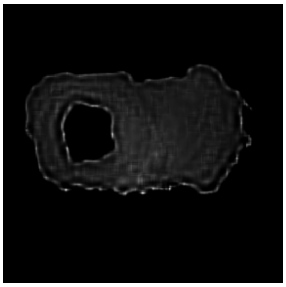

(c) Deconvoluted image (grayscale)

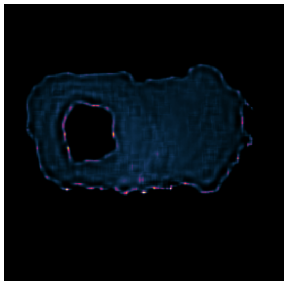

(d) Deconvoluted image (fire colormap)

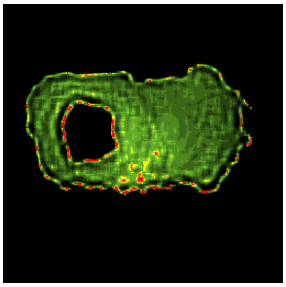

(e) Deconvoluted image (custom colormap), threshold of 0.11 and 0.14

Figure 4.13: The effect of spatially variant deconvolution on tissue with an image size of 256x256 after 10 iterations.

4.4 Discussion

In this study, we investigated whether space-variant deconvolution could be applied to fluorescence images to correct for the blurring effect of scattering. Our result show that a first step in spatially-variant deconvolution is taken, but that result is dependent on multiple assumptions, making it prone to inaccuracies.

Our findings show that segmentation is possible based on the HSV image and that the corresponding scattering coefficient can be assigned to these segmented tissues. However, the segmentation is based on intensity and visualization of the tissue and not strictly on the tissue itself. This could cause assigning the wrong sigma to a pixel. Furthermore, the scattering coefficient of tissue at the specific wavelength (760 nm) is not always accurate. Often, the scattering coefficient must be calculated for the specific wavelength or multiple scattering coefficients are available for the same tissue. Therefore, an assumption must be made for each scattering coefficient. Next, assumed is that the source for the scattering lies in the middle of the bread loaf slice. In reality, these sources can lie at multiple depths, therefore influencing the used sigma. Both steps introduce inaccuracies in assigning the right amount of blurring per pixel. An improvement could be to use MDSFR-SFF spectroscopy to measure the scattering and absorption coefficient of multiple tissues within the slice. These coefficients could be averaged, to get a final scattering and absorption coefficient for a specific tissue at a specific wavelength.

For spatially-invariant deconvolution, both the original Richardson-Lucy method and our method showed similar images, indicating comparable methods when using only one sigma. Furthermore, the effect of the kernel size to the deconvolution was shown. As two sigma's are assigned to the pixels and only one kernel sized was used, some pixels will be deconvolved with a suboptimal kernel size, resulting in artefacts

Spatially-variant deconvolution of the phantom showed an increase in sharpness, but also induced artefacts. These could be the result of ringing, but also deconvolution with a suboptimal kernel size. The spatially-variant deconvolution of the tissue showed an improvement of the fluorescent image, but was not very trustworthy. Further research could maybe improve the images and reduce the artefacts. One of the main drawbacks of the spatially-variant methods, especially clinically, is the computation time of the algorithm. Due to the computation time, the images were already resized from 512x512 to 256x256. For the resized image, the general computation time was between 60 and 90 minutes. For an image of 512x512 this exceeded 24 hours. Therefore, it should be considered if the results are worth the computation time.

The before mentioned inaccuracies in segmentation of the tissue, definition of the deconvolution variables and deconvolution artefacts make it challenging to make a clear interpretation of the results. Although a certain amount of uncertainty will always be present in the ill-posed deconvolution, more accurate methods are necessary for tissue segmentation and definition of the sigma to be able to implement it clinically. At this moment, it would still be difficult to implement this method to a more clinically available method, as it does not reduce the unknown variables in the fluorescence images.

4.5 Conclusion

This study shows that the adjusted spatially variant deconvolution algorithm is working, in a way, that it generates deconvolved images. However, the images are suffering from artefacts and especially the deconvolved tissue image. These artefacts are probably the result of the applied Richardson-Lucy algorithm, but also due to the multiple assumptions that are made for the deconvolution. It should be questioned if the result and possible interpretation of these results is worth the time required for the correction.

5 | General Conclusions

This study, consisting of three substudies, showed that an optimal correction for fluorescence images is still difficult. The ratiometric correction method showed that an improvement of the fluorescence image can be reached and that an absolute colormap per tissue type is possible. This correction method could improve fluorescence visualization for both intraoperative and endoscopic imaging. However, more research is necessary to find optimal thresholds and to be able to implement it clinically. The spatially variant deconvolution is more complicated. The method used multiple assumptions according to the blurring effect per pixel, resulting in possible inaccuracies in the method. Furthermore, the Richardson-Lucy deconvolution also induces ringing artefacts, resulting in more decrease of the deconvolved image. It should be questioned if the result and possible interpretation of these results is worth the acquisition time for the correction.

Bibliography

[1] T. E. Bernstein, B. H. Endreseth, P. Romundstad, and A. Wibe, "Circumferential resection margin as a prognostic factor in rectal cancer," *British Journal of Surgery*, vol. 96, no. 11, pp. 1348–1357, 2009.

[2] A. Wibe, P. R. Rendedal, E. Svensson, J. Norstein, T. J. Eide, H. E. Myrvold, and O. Sùreide, "Prognostic significance of the circumferential resection margin following total mesorectal excision for rectal cancer," *British Journal of Surgery*, vol. 89, pp. 327–334, 2002.

[3] Integraal kankercentrum Nederland, "Oncoline," 2016.

[4] A. L. Vahrmeijer, M. Hutteman, J. R. Van Der Vorst, C. J. H. Van De Velde, A. L. Vahrmeijer, M. Hutteman, J. R. Van Der Vorst, C. J. H. Van De Velde, and J. V. Frangioni, "Image-guided cancer surgery using near-infrared fluorescence," *Nature Reviews - Clinical Oncology*, vol. 10, pp. 507–518, 2013.

[5] D. Holt, A. B. Parthasarathy, O. Okusanya, J. Keating, O. Venegas, C. Deshpande, G. Karakousis, B. Madajewski, A. Durham, S. Nie, A. G. Yodh, and S. Singhal, "Intraoperative near-infrared fluorescence imaging and spectroscopy identifies residual tumor cells in wounds," *Journal of Biomedical Optics*, vol. 20, no. 7, p. 076002, 2015.

[6] Breastcancer.org, "Your Guide to the Breast Cancer Pathology Report," 2006.

[7] E. De Boer, N. J. Harlaar, A. Taruttis, W. B. Nagengast, E. L. Rosenthal, V. Ntziachristos, and G. M. Van Dam, "Optical innovations in surgery," *British Journal of Surgery*, vol. 102, no. 2, pp. 56–72, 2015.

[8] A. Kleespies, M. Guba, K.-W. Jauch, and C. J. Bruns, "Vascular endothelial growth factor in esophageal cancer," *Journal of Surgical Oncology*, vol. 87, no. 2, pp. 95–104, 2004.

[9] W. B. Nagengast, E. G. de Vries, G. A. Hospers, N. H. Mulder, J. R. de Jong, H. Hollema, A. H. Brouwers, G. A. van Dongen, L. R. Perk, and M. N. Lub-de Hooge, "In Vivo VEGF Imaging with Radiolabeled Bevacizumab in a Human Ovarian Tumor Xenograft," *Journal of Nuclear Medicine*, vol. 48, no. 8, pp. 1313–1319, 2007.

[10] V. Ntziachristos, "Going deeper than microscopy: the optical imaging frontier in biology.," *Nature methods*, vol. 7, no. 8, pp. 603–614, 2010.

[11] P. van Driel, S. Keereweer, T. Snoeks, and C. Löwik, "Fluorescence-Guided Surgery: A Promising Approach for Future Oncologic Surgery," in *Reference Module in Biomedical Sciences*, vol. 4, pp. 301–333, Elsevier B.V., 2014.

[12] A. E. F. Taylor, J. Bailey, and J. Gross, *Illumination Fundamentals*. Rensselaer PolyTechnic Institute, 2000.

[13] S. Keereweer, P. B. A. A. Van Driel, T. J. A. Snoeks, J. D. F. Kerrebijn, R. J. B. De Jong, A. L. Vahrmeijer, H. J. C. M. Sterenborg, and C. W. G. M. Löwik, "Optical image-guided cancer surgery: Challenges and limitations," *Clinical Cancer Research*, vol. 19, no. 14, pp. 3745–3754, 2013.

[14] W. M. Star, P. Med, O. Barajas, Å. M. Ballangrud, G. Miller, E. Torres-garcía, and W. M. Star, "Physics in Medicine & Biology Related content Light dosimetry in vivo in biological tissue Light dosimetry in vivo," *Physics in Medicine and Biology*, vol. 42, pp. 763–787, 1997.

[15] T. Vo-dinh, *Biomedical Photonics handbook*. CRC Press, 2003.

[16] R. S. Bradley and M. S. Thorniley, "A review of attenuation correction techniques for tissue fluorescence.," *Journal of the Royal Society, Interface / the Royal Society*, vol. 3, no. August 2005, pp. 1–13, 2006.

[17] A. J. Welch and M. J. C. van Gemert, *Optical-Thermal Response of Laser-Irradiated Tissue*. Springer US, 2011.

[18] J. H. Lee and T. D. Wang, "Molecular endoscopy for targeted imaging in the digestive tract," *The Lancet Gastroenterology & Hepatology*, vol. 1, no. 2, pp. 147–155, 2016.

[19] G. Lu and B. Fei, "Medical hyperspectral imaging: a review.," *Journal of biomedical optics*, vol. 19, no. 1, p. 10901, 2014.

[20] J. V. Frangioni, "In vivo near-infrared fluorescence imaging," *Current Opinion in Chemical Biology*, vol. 7, no. 5, pp. 626–634, 2003.

[21] R. Weissleder, "A clearer vision for in vivo imaging Progress continues in the development of smaller , more penetrable probes for biological imaging . Toward the phosphoproteome," *Nature Biotechnology*, vol. 19, no. 4, pp. 316–317, 2001.

[22] J. R. Lorenzo, "Light Absorbers, Emitters and Scatterers: The Origins of Color in Nature," in *Principles of diffuse light propagation: light propagation in tissues with applications in biology and medicine*, pp. 3–51, World Scientific, 2012.

[23] B. Yang, M. Sharma, J. W. Tunnell, B. Yang, M. Sharma, and J. W. Tunnell, "Attenuation-corrected fluorescence extraction for image-guided surgery in spatial frequency domain," *Journal of Biomedical Optics*, vol. 18, no. 8, p. 80503, 2013.

[24] J. Vervandier and S. Gioux, "Single snapshot imaging of optical properties.," *Biomedical optics express*, vol. 4, no. 12, pp. 2938–44, 2013.

[25] J. Sun, D. Hathi, H. Zhou, M. Shokeen, and W. J. Akers, "Enhancing contrast and quantitation by spatial frequency domain fluorescence molecular imaging," *SPIE*, vol. 9715, p. 97150Y, 2016.

[26] T. O'Sullivan, "Diffuse optical imaging using spatially and temporally modulated light," *Journal of Biomedical Optics*, vol. 17, no. 7, p. 071311, 2012.

[27] A. M. Laughney, V. Krishnaswamy, T. B. Rice, D. J. Cuccia, R. J. Barth, B. J. Tromberg, K. D. Paulsen, B. W. Pogue, and W. A. Wells, "System analysis of spatial frequency domain imaging for quantitative mapping of surgically resected breast tissues," *Journal of Biomedical Optics*, vol. 18, no. 3, p. 036012, 2013.

[28] D. Cuccia, F. Bevilacqua, A. J. Durkin, F. R. Ayers, and Bruce J., "Quantitation and mapping of tissue optical properties using modulated imaging," *Journal of Biomedical Optics*, vol. 14, no. 2, pp. 1–31, 2009.

[29] V. Ntziachristos, G. Turner, J. Dunham, S. Windsor, A. Soubret, J. Ripoll, and H. a. Shih, "Planar fluorescence imaging using normalized data.," *Journal of biomedical optics*, vol. 10, no. 6, p. 064007, 2005.

[30] B. P. Joshi, Z. Dai, Z. Gao, J. H. Lee, N. Ghimire, J. Chen, A. Prabhu, E. J. Wamsteker, R. S. Kwon, G. H. Elta, E. M. Stoffel, A. Pant, T. Kaltenbach, R. M. Soetikno, H. D. Appelman, R. Kuick, D. K. Turgeon, and T. D. Wang, "Detection of Sessile Serrated Adenomas in Proximal Colon Using Wide-Field Fluorescence Endoscopy," *Gastroenterology*, no. February, pp. 1–12, 2016.

[31] B. P. Joshi, X. Duan, R. S. Kwon, C. Piraka, B. J. Elmunzer, S. Lu, and E. F. Rabinsky, "Multimodal endoscope can quantify wide-field fluorescence detection of Barrett ' s neoplasia," *Endoscopy International Open*, 2015.

[32] G. Themelis, J. S. Yoo, K.-S. Soh, R. Schulz, and V. Ntziachristos, "Real-time intraoperative fluorescence imaging system using light-absorption correction.," *Journal of biomedical optics*, vol. 14, no. 6, p. 064012, 2009.

[33] V. Ntziachristos, "Clinical translation of optical and optoacoustic imaging," *Philosophical Transactions of the Royal Society A: Mathematical, Physical and Engineering Sciences*, vol. 369, no. 1955, pp. 4666–4678, 2011.

[34] J. T. Bushberg, "Image Quality," in *The essential physics of medical imaging*, vol. 2, ch. Image Qual, pp. 37–59, Wolters Kluwer, 2015.

[35] J. Glatz, *Real-time intra-operative and endoscopic molecular fluorescence imaging*. PhD thesis, Technical univeristy of München, 2015.

[36] H. L. Yang, P. H. Huang, and S. H. Lai, "A novel gradient attenuation Richardson-Lucy algorithm for image motion deblurring," *Signal Processing*, vol. 103, pp. 399–414, 2014.

[37] T. R. Lauer, "Deconvolution With a Spatially-Variant PSF," *Arxiv preprint astroph0208247*, vol. 4847, no. 520, p. 7, 2002.

[38] S. L. Jacques, "Optical properties of biological tissues: A review," *Physics in Medicine and Biology*, vol. 58, no. 11, 2013.

[39] S. Carvalho, N. Gueiral, E. Nogueira, R. Henrique, L. Oliveira, and V. V. Tuchin, "Comparative study of the optical properties of colon mucosa and colon precancerous polyps between 400 and 1000 nm," *Proc. of SPIE*, vol. 10063, p. 100631L, 2017.

[40] D. S. C. Biggs and M. Andrews, "Acceleration of iterative image restoration algorithms," *Applied Optics*, vol. 36, p. 1766, mar 1997.